A characteristic mapping method for the incompressible Euler equations on a sphere

Department of Mathematics and Statistics
McGill University, Montreal
December 2020

A thesis submitted to McGill University in partial fulfillment of the

requirements of the degree of Master of Science in Mathematics and Statistics

Abstract

In this thesis, analytical and numerical aspects of the solution to the incompressible Euler equations on a two-dimensional sphere using the Characteristic Mapping (CM) method are presented. These equations dictate the time evolution of an incompressible, inviscid fluid from a prescribed initial condition. Their non-linear nature produces increasingly fine scales over time; posing a challenge for existing numerical methods. This problem is broached using the CM method, which considers the numerical quantity of interest to be the flow map generated by the fluid motion. The semigroup property of the flow map, facilitating its own evolution by means of composition, is leveraged to capture the fine scales manifest in the dynamics of the fluid. We begin with a presentation of the vorticity-stream formulation of the incompressible Euler equations on a sphere, from which the solution strategy is built. An implementation for solving the spherical Poisson equation using the double Fourier sphere method is presented. Thereafter, the CM method for linear transport on the 2-sphere is presented. The thesis is concluded with a discussion of combining these two numerical methods for the solution of the incompressible Euler equations.

Abrégé

Dans cette thèse, les aspects analytiques et numériques du solution des équations d'Euler incompressibles sur une sphère deux dimensionelles en utilisant la méthode d'application des caractéristiques (AC) sont présentées. Ces équations dictent l'évolution d'une fluide incompressible et non-visqueux d'une état initiale donné. La nature non-linéaire de l'écoulement se produit des échelles fines dans la fluid au fil du temps; posant des difficultés pour les méthodes numériques existantes. Cette problème est addressé en utilisant la méthode AC, qui considère la quantité d'intéresse d'être l'application du flot généré par la vitesse du fluide. La propriété semi-groupe de l'application du flot, facilitant sa propre évolution par composition, est utilisée pour résoudre des échelles fines inhérent aux dynamiques du fluide. On commence avec un présentation du vorticité-courant formulation des équations d'Euler incompressibles sur une sphère, à laquelle notre stratégie de solution est construite. Une implémentation de la double Fourier sphère pour la solution de l'équation Poisson sphérique est présentée. Par la suite, la méthode AC pour l'équation du transport linéaire sur la 2-sphère est présentée. La thèse se conclut avec une discussion des aspects de combiner ces deux méthodes pour la solution des équations d'Euler incompressibles.

Acknowledgements

The research presented in this thesis would have not been possible without the people who have graciously given their time and shared their knowledge on its subject matter. Firstly, I would thank my supervisor, Jean-Christophe Nave. His perspectives on teaching and research in mathematics were instrumental in the success of this project. I am grateful for the careful attention to the scientific method that he has fostered throughout this project. I would also like to thank my co-supervisor Gantumur Tsogtgerel for his exceptional teaching on partial differential equations and approximation theory.

A special thanks to Jean-Christophe's research group for their support and camaraderie. I am especially appreciative for the guidance that Xi Yuan-Yin has provided on my code for the implementation of the Characteristic Mapping method and his willingness to answer my many questions.

I am eternally grateful for the love and support my friends and family have shown me throughout all of my studies. Their encouragement and shared laughter could never be overlooked.

The numerical methods presented are largely based on the work of Montanelli et al. [38] in Chapter 2 and Mercier et al. [36], Yin et al. [74], and Nave et al. [44] in Chapter 3. The work presented in Chapter 4 and the application of the Characteristic Mapping method on a spherical geometry is the work of the author.

" *What goes around is all around.*"

- Old Canadian proverb

Contents

List of Figures

Chapter 1

Mathematical Framework

1.1 Introduction

In 1761, Leonhard Euler derived the equations of motion for an incompressible and inviscid fluid [18]. To this day, these equations still pose a challenge in both pure and applied mathematics. It remains an open question in fluid dynamics whether or not the incompressible Euler equations in three dimensions develop a singularity in the vorticity field in finite time. It has not been answered definitively whether the accumulation of the vorticity exhibits a growth that is exponential or even double-exponential in time [25]. The presence of the fast growing vorticity field generates increasingly fine-scales in the vorticity overtime; posing a challenge for their numerical solution.

The simulation of the incompressible Euler equations has great utility to the applied scientist. Dynamical processes governed by fluid motion are ubiquitous in almost every scientific discipline. Although idealized, Euler's equations still provide insight into the complex nature of continuum motion. In cosmology, the Euler-Poisson system, which couples the motion of an incompressible fluid transporting mass with gravitational attraction is being used to better understand large-scale structure formation in the universe [50]. The simulation of Euler's equations on a rotating sphere is used to better understand the atmospheric dynamics on planets in our solar system [23]. A pressing application on Earth, is their use as part of the shallow-water equations, which are currently used in operational models for numerical weather prediction [33]. Overcoming computational issues related to high-resolution simulations will allow applied scientists to better evaluate error in their models of anthropogenic climate change [3], thereby permitting a more reliable quantification of our impact on Earth's atmosphere and climate [39].

Motivated by these applications to problems involving spherical geometries, we consider the numerical solution of the incompressible Euler equations on the 2-sphere. Due to the lack of vortex-stretching in two-dimensions, the sup-norm of the gradient of the vorticity can be bound by a double exponential in time [75], and thus does not exhibit the same growth behaviour as in the three-dimensional case. Nevertheless, these still fast growing gradients in two-dimensions still poses a challenge to the computational fluid dynamics community.

We begin with a discussion of the mathematical framework for the problem on an arbitrary compact Riemannian 2-manifold. Firstly, we provide a review of the properties of flows of vector fields on smooth manifolds. Thereafter, a derivation of the incompressible Euler equations on a compact Riemannian 2-manifold is presented. Finally, we discuss the vorticity-stream formulation from which our numerical solution strategy is built.

1.2 Flows on bounded manifolds

A fundamental object to the Characteristic Mapping method is the flow map generated by the velocity field. We begin by discussing some of the properties of flows on compact, smooth manifolds, similar to the discussion found in [1]. Let the fluid domain, M, be a Riemannian n-manifold, and let $p \in M$ be a point on M. Consider local coordinate charts (φ_i, U_i), $i = 1, \ldots, N$, with open sets $U_i \subseteq M$ such that their union covers M and that the transition maps $\psi_{i,j} = \varphi_i \circ \varphi_j^{-1} : \varphi_j(U_i \cap U_j) \to \varphi_i(U_i \cap U_j)$ are differentiable with smooth inverses. Local coordinates of $p \in U_i$ will be denoted $x = \varphi_i(p)$. Let $u : M \times \mathbb{R} \to TM$, where TM is the tangent bundle of M, be a time-dependent vector field on M, defining the time-evolution of the velocity field in the fluid. We begin by studying the time-independent case, for $u \in \mathfrak{X}(M)$, where $\mathfrak{X}(M)$ is the set of all C^∞ vector fields on M, and thereafter relating their properties to the time-dependent case. Since a vector field assigns a tangent vector to every point $p \in M$, we may consider the curves on M whose tangent vectors coincide with the vector field.

Definition 1.1 (Integral curve)**.** Let $I \subset \mathbb{R}$ be an open interval containing 0. The curve $\gamma : I \to M$, is called an *integral curve* of the vector field $u \in \mathfrak{X}(M)$ at $p \in M$ if γ is the solution to the initial value problem

$$\frac{d\gamma}{dt}(t) = u(\gamma(t)), \quad \gamma(0) = p, \quad \forall t \in I \tag{1.1}$$

These curves define trajectories of a 'particle' passively transported by the fluid. We recall that a curve γ on M passing through p is defined as a map $\gamma : I \to M$ such that

$\gamma \in C^1(I; M), \gamma(0) = p$. The map assigning to every $p \in U_i$ the integral curve satisfying 1.1 is the *local flow map* of u in U_i. The existence and uniqueness of integral curves and properties of the local flow map follow from considering the local representative in coordinates of the solution curve and applying the Picard-Lindelöf theorem. Before quantifying this proposition, we establish a uniqueness result.

Theorem 1.1 (Global uniqueness)**.** Let γ_1, γ_2 be two integral curves of a vector field $u \in \mathfrak{X}(M)$ at a point $p \in M$. Then $\gamma_1 = \gamma_2$ on the intersection of their domains.

Proof. We note that generally the local representatives, γ_1, γ_2 will lie in different coordinate charts. Let $I_1, I_2 \subseteq \mathbb{R}$ such that $0 \in I_1, I_2$, suppose $\gamma_1 : I_1 \to M$ and $\gamma_2 : I_2 \to M$. Denote $I = I_1 \cap I_2$ and let $J = \{t \in I \,|\, \gamma_1(t) = \gamma_2(t)\}$, which is non-empty since the integral curves agree at $p \in M$, i.e. $\gamma_1(0) = \gamma_2(0) = p$. The set J is closed since γ_1, γ_2 are continuous. We want to show that J is also open, and thus $J = I$. Considering the local representatives of the integral curves, since they both satisfy 1.1, then by Picard-Lindelöf we have that $\exists\ (-\epsilon, \epsilon) \in J$. Let $t \in J$, then we have that $\gamma_1(t + s)$ and $\gamma_2(t + s)$ are both integral curves at $\gamma_1(t) = \gamma_2(t)$. Using Picard-Lindelöf once again, we have that $\exists$ $(-\delta(t), \delta(t)) \in J$ where they agree, thus we have an open neighbourhood of every $t \in J$ that is contained in J. □

Lemma 1.2. Let $u \in \mathfrak{X}(M)$, $U_0 \in M$ open, and $I_c = (-c, c)$ where $c > 0$ is a constant depending on the size of U_0. Let $X : U_0 \times I_c \to M$ be the local flow map such that for each $p \in U_0$ and curve $\gamma : I_c \to M$ defined by $X_t(p) = X(\gamma(0), t) = \gamma(t)$ is an integral curve of u at p. Then for t, s such that $t + s \in I_c$ we have that,

$$\begin{aligned} X_{t+s} &= X_t \circ X_s = X_s \circ X_t \,, \\ X(\cdot, 0) &= \mathrm{id}_M \,, \end{aligned} \tag{1.2}$$

where id_M is the identity map on M. Moreover, if $U(t) = X(U_0, t)$ and $U(t) \cap U_0 \neq \emptyset$, then $X_{-t} = X_t^{-1} : U(-t) \cap U_0 \to U_0 \cap U(t)$ is the inverse of X.

Proof. We have that $X_{t+s}(\gamma)$ is the integral curve of u at $p \in M$ and by definition of X we have that $X_t(X_s(\gamma)) = X_t(\gamma(s))$ which is also an integral curve at p. Therefore, by 1.1 we have that $X_t(X_s(\gamma)) = X_{t+s}(\gamma)$. Moreover, we have that $X_{t+s}(\gamma) = X_{s+t}(\gamma) = (X_s \circ X_t)(\gamma)$. Since $\gamma(0) = p$ we readily have $X_0(\gamma) = p \Rightarrow X_0 = \mathrm{id}_M$. The inverse property then follows from noting $X_{t-t} = X_t \circ X_{-t} = X_{-t} \circ X_t = \mathrm{id}_M$. □

Theorem 1.3 (Existence and uniqueness)**.** Let $u \in \mathfrak{X}(M)$, for every $p \in M$ there exists a triple (U_0, c, X) satisfying the properties of 1.2. Moreover, if (U_0', c', X') and (U_0, c, X)

both satisfy the properties of 1.2 at p, then $X = X'$ on $(U_0 \cap U_0') \times (I_c \cap I_{c'})$ and X is a smooth diffeomorphism.

Proof. Consider a point $p \in U_0 \cap U_0'$, since X, X' are both local flow maps for u, we have that $X = X'$ on $\{p\} \times (I_c \cap I_{c'})$ and thus $X = X'$ on $(U_0 \cap U_0') \times (I_c \cap I_{c'})$ using 1.1.

Existence follows from using a local representative in $\mathbb{R}^n$. Let (φ_i, U_i) be a chart on M. Let $p \in U_i$, and let $U_0 \subset U_i$ open, since X is continuous $\exists\, b \in (0, c)$ and $V_0 \subset U_0$ where $p \in V_0$ such that $X(U_0, (0, b)) \subset U_0$. Since the functions φ_i, by definition of a chart, are smooth in an open neighbourhood around $p \in U_i$ with smooth inverses, we may relate 1.1 to the ordinary differential equation,

$$\frac{d}{dt}\left(\varphi_i \circ \gamma\right)(t) = u(\varphi_i \circ \gamma, t)\ ,\ \left(\varphi_i \circ \gamma\right)(0) = \varphi_i(p) \tag{1.3}$$

By application of Picard-Lindelöf there is an open neighbourhood $t \in (-\epsilon, \epsilon)$ on which a unique solution to1.3 exists. Let u' and X_t' be the local representatives of the velocity field and the flow map respectively. Then the flow map itself can be defined by left composition with ϕ_i^{-1}, i.e.

$$X : U_0 \times I_c \to M; \quad (p, t) \mapsto \varphi_i^{-1}(X'(\varphi_i(p), t)) \tag{1.4}$$

Picard-Lindelöf gives us that $\exists$ an open neighbourhood U'about $\varphi_i(p)$ and an $\epsilon > 0$ such that $X_t'(\varphi_i(p), t) = (\varphi_i \circ \gamma)(t)\, \forall t \in (-\epsilon, \epsilon)$, where $(\varphi_i \circ \gamma)(t)$ is the solution to 1.3. We obtain $V_0 = \varphi_i^{-1}(U')$ which is open since φ_i^{-1} is continuous. Moreover, the local flow map is a diffeomorphism since u' is smooth and hence and it follows that the composition $X(p, t) = (\varphi_i^{-1} \circ X')(\phi(p), t)$ is also smooth with smooth inverse. By the properties of 1.2, X_t is a diffeomorphism with inverse X_{-t}. □

To extend these local considerations to global ones, for flow maps defined over the entire manifold, we must use the notion of completeness. We suppose now that the manifold M is a compact manifold. A vector field $u \in \mathfrak{X}(M)$ is called *complete* if the solution curves exist for all time.

Proposition 1.1. Every vector field on a compact manifold is complete.

Proof. Since M has compact support and $u : M \to TM$, u has compact support. For every $p \in M$ we can consider integral curves, $\gamma_p(t)$ such that $\gamma(0) = p$. By the previous existence and uniqueness theorems, there is an open neighbourhood U_p of every p such that $\gamma(t)$ satisfies 1.1 for $t \in (-\epsilon(p), \epsilon(p))$. The collection of all such U_p covers M and since M is compact, there is a finite subcover $V_{\epsilon(p)}$ of M. Since $V_{\epsilon(p)}$ is finite, we take ε to

be the smallest such $\epsilon(p)$ and thus $\gamma_p(t)$ exists $\forall t \in (-\varepsilon, \varepsilon)$. Now suppose there was some $p' \in M$ such that the interval of existence of the integral curve $\gamma_{p'}(t)$, where $\gamma(0) = p'$ was finite; call the maximal solution time T. The point $q = \gamma_{p'}(T) \in M$, and since $V_{\epsilon(p)}$ covers M, we have that the curve $\tilde{\gamma}_{p'}(t) = \gamma_{p'}(T + t)$ is an integral curve with initial condition $\tilde{\gamma}_{p'}(0) = q$ and exists for $t \in (-\epsilon, \epsilon)$ by construction of $V_{\epsilon(p)}$ which contradicts T being the maximal solution time. □

Having now established global existence and uniqueness of integral curves for a smooth vector field u on a compact manifold M, we now wish to relate these notions to the time-dependent case. We begin with the definition of a time-dependent flow.

Definition 1.2 (Time-dependent flow)**.** For $u \in \mathfrak{X}(M; \mathbb{R})$, we define the vector the time-dependent flow $X_{t,s} : (M \times \mathbb{R}) \times \mathbb{R} \to M \times \mathbb{R}$ is defined such that, $X((\gamma(t), t), s) = (\gamma(s), s)$ where $(\gamma(s), s)$ is the integral curve satisfying the non-autonomous differential equation,

$$\dot{\gamma}(s) = u(\gamma(s), s), \quad (\gamma(0), 0) = (p, t) \tag{1.5}$$

The flow property from before is replaced by the property $X_{t,s} \circ X_{s,r} = X_{t,r}$ and $X_{t,t} = \mathrm{id}_M$. For fixed time s, $X_{t,s}$ is the flow map for the vector field $u(s) \in \mathfrak{X}(M)$.

The time-independent case encompasses the time-dependent case by the vector field $\tilde{u}$ as

$$\tilde{u}(s, p) = \left(\left. \frac{\partial}{\partial s} \right|_s , u(s, p) \right) \tag{1.6}$$

where the time-dependence has been parameterized. The vector field $\tilde{u}$ can be seen as a time-independent vector field on the larger manifold $\mathbb{R} \times M$ whose tangent space is given by $T_{(s,p)}(\mathbb{R} \times M) \cong T_s\mathbb{R} \times T_pM$. This allows us to consider the integral curves 1.5 as a system of autonomous ordinary differential equations. Consequently, the flow of the time-dependent vector field can be written as $X_t(s, p) = (t + s, X_{t+s,s}(p))$, with inverse, $X_{-t}(s, p) = (s - t, X_{s-t,s}(p))$. If we restrict ourselves to time-dependent vector fields which are also continuous in time, then on the product space, the flow $X_t(s, p)$ enjoys the same properties as in the time-independent case described above. Though, we are not guaranteed global existence of integral curves on the product space since $\mathbb{R} \times M$ is no longer compact.

We will use the flow map and its inverse in the derivation of the incompressible Euler equations. For integral quantities in the fluid domain such as mass and momentum, we require the pull-back with respect to the flow map.

Definition 1.3 (Pull-Back)**.** Let $f \in C^\infty(M)$ and let α be a k-form on M, that is $\alpha \in \Omega^k(M)$. The pull-back of α by f, denoted $f^*\alpha$ is a k-form on M, for $p \in M$ is given by

$$(f^*\alpha)_p(v_1, \ldots, v_k) = \alpha_{f(p)}(T_p f \cdot v_1, \ldots, T_p f \cdot v_k) \tag{1.7}$$

The pull-back of a k-form and the Lie derivative of a k-form are related as follows,

Definition 1.4 (Lie derivative)**.** Let $\alpha \in \Omega^k(M)$, $u \in \mathfrak{X}(M;\mathbb{R})$ then the Lie derivative of α along u is given by,

$$\pounds_{u(t)}\alpha = \left.\frac{d}{ds}\right|_{s=t} X_{s,t}^*\alpha \tag{1.8}$$

Using this definition and the definition of the pull-back, we have the following theorem

Theorem 1.4. Let $\alpha \in \Omega^k(M)$ and $u \in \mathfrak{X}(M;\mathbb{R})$ be with associated time-dependent flow $X_{t,s} : \mathbb{R} \times (\mathbb{R} \times M) \to \mathbb{R} \times M$, then the following holds,

$$\frac{d}{dt} X_{t,s}^*\alpha = X_{t,s}^* \pounds_{u(t)}\alpha \tag{1.9}$$

Proof. Using the definition 1.4, and the fact the $X_{t,t} = \mathrm{id}_M$, we have that,

$$\frac{d}{dt} X_{t,s}^*\alpha = \left.\frac{d}{dr}\right|_{r=s} (X_{r,t} \circ X_{t,s})^* (\alpha) = X_{t,s}^* \left(\left.\frac{d}{dr}\right|_{r=t} X_{r,t}^*\alpha \right) = X_{t,s}^* \pounds_{u(t)}(\alpha) \tag{1.10}$$

□

The divergence of a vector field is defined using the Lie derivative, namely:

Definition 1.5 (Divergence)**.** Let μ be the volume form on M induced by the metric tensor. The unique function $\mathrm{div}(u) \in C^\infty(M)$, such that $\pounds_u(\mu) = \mathrm{div}(u)\mu$ is called the divergence of u.

Incompressible fluid flow conserves the volume of any given region and is a consequence of a divergence free velocity field. To observe this fact, let $U_0 \subset M$ be a fixed region and denote $U(t) = X(U,t)$ the region flowing with the fluid. Let $\mathrm{div}(u)d\mu = 0$, where $d\mu$ is a volume form on M. Then we have that

$$\begin{aligned} \frac{d}{dt}\int_{U(t)} d\mu &= \int_{U_0} \frac{d}{dt} X^*(d\mu) = \int_{U_0} X^*\left(\pounds_u d\mu\right) \\ &= \int_{U(t)} \mathrm{div}(u) d\mu = 0\,, \end{aligned} \tag{1.11}$$

where we have used 1.4 and 1.5. Using this fact, we deduce

$$\begin{aligned} \int_{U(t)} d\mu &= \int_{U_0} X^*(d\mu) = \int_{U_0} \det\left(\nabla X\right) d\mu \\ &= \int_{U_0} d\mu \iff \det\left(\nabla X\right) = 1\,, \quad \forall t \in \mathbb{R} \end{aligned} \tag{1.12}$$

that is, a divergence free-condition on the velocity field is equivalent to the condition $\det(\nabla X) = 1$ for all time.

1.3 Incompressible Euler Equations

We present a derivation of the incompressible Euler on a compact Riemannian 2-manifold M that is diffeomorphic to the 2-sphere. The equations of motion for an incompressible, inviscid fluid follow from evoking conservation of mass and momentum balance on a model of a continuum system defined by the fluid velocity, pressure, and density. If u denotes the fluid velocity, then the trajectory of a 'particle' of the fluid that was at x at time $t = 0$ is given by $X(x(t), t)$, where X is the time-dependent flow map of the velocity field. Let $g : T_pM \times T_pM \to \mathbb{R}$ be the Riemannian metric defined on M. We note that the volume form $d\mu$ on M, in local coordinates, is given by $d\mu = \sqrt{|g|}dx^1 \wedge \cdots \wedge dx^n$ where $|g|$ is the absolute value of the determinant of g. The Eulerian and Lagrangian velocities are given by $u(x,t)$ and $\dot{X}(x,t) = u(X(x,t),t)$ respectively. We see that the fluid flow map and its inverse serve as a means of transformation between each frame of reference.

A fundamental notion in continuum mechanics is the advection or transport of a quantity under a given velocity field. Advected quantities may be passive; where they are carried along by the fluid flow without interacting with it, or active; where they dynamically interact with and change the medium in which they are being transported. The former of these two cases is characterized by the following theorem,

Theorem 1.1 (Transport Theorem)**.** Let M be a manifold equipped with volume form $d\mu$ and let $u \in \mathfrak{X}(M;\mathbb{R})$ be a time-dependent vector field with flow map $X : M \times \mathbb{R} \to M$. Let $\phi : M \times \mathbb{R} \to \mathbb{R}$ be a scalar field and consider $U \subset M$ then we have

$$\frac{d}{dt}\int_{X(U,t)} \phi d\mu = \int_{X(U,t)} \left(\frac{\partial \phi}{\partial t} + \mathrm{div}(\phi \boldsymbol{u})\right) d\mu \tag{1.13}$$

Proof. The proof follows directly from 1.4 and the definition of the divergence of u 1.5. Namely, we have

$$\begin{aligned} \frac{d}{dt}\int_{X(U,t)} \phi d\mu &= \int_U \frac{d}{dt} X^* (\phi d\mu) = \int_U X^* \left(\pounds_u(\phi d\mu) + \frac{\partial \phi}{\partial t} d\mu\right) \\ &= \int_U X^* \left((u(\phi) + \phi \mathrm{div} u + \frac{\partial \phi}{\partial t})d\mu\right) = \int_{X(U,t)} \left(\frac{\partial \phi}{\partial t} + \mathrm{div}(\phi u)\right) d\mu\,, \end{aligned} \tag{1.14}$$

which establishes the theorem. □

We evoke the continuum assumption, and assume that the fluid's mass can be characterized by a smooth mass density function $\rho : M \times \mathbb{R} \to \mathbb{R}$, such that the mass in

a given region $U \subset M$ in the fluid domain is given by:

$$m(U,t) = \int_U \rho d\mu \tag{1.15}$$

In the absence of sinks or sources, conservation of mass states that the mass of a fluid in region U, transported with the flow, remains constant over time. More concretely, we can show that the mass density obeys a continuity equation,

$$\frac{d}{dt}\int_{X(U,t)} \rho d\mu = 0 \Rightarrow \frac{\partial \rho}{\partial t} + \mathrm{div}(\rho \boldsymbol{u}) = 0\,, \tag{1.16}$$

by using 1.1 and the fact that ρ was assumed to be smooth. Having evoked conservation of mass, we now consider Newton's second law. Since the fluid has mass, it has a means of transferring momentum within itself, described by some force. The Cauchy stress tensor, σ encapsulates the forces of stress and strain acting on a region of the fluid. Let U be an arbitrary region within the fluid, and denote by da the volume element induced on ∂U. Then the internal forces of the fluid acting on U are given by,

$$F = \int_{\partial X(U,t)} \sigma(x,t) \cdot \boldsymbol{n}\, da\,. \tag{1.17}$$

An *ideal fluid* is defined such that the internal forces only act upon the normal direction to the region U. The stress tensor then reduces to the form $\sigma^{i,j} = -p(x,t)g^{i,j}$ where p is a scalar function called the pressure and $g^{i,j}$ is the inverse metric tensor. Noting that the momentum density is given by the product of the velocity field with the mass density, Newton's II law for an ideal fluid in the absence of external forces, is given by,

$$\frac{d}{dt}\int_{X(U,t)} \rho u\, d\mu = -\int_{\partial X(U,t)} p(x,t)\boldsymbol{n}\, da \tag{1.18}$$

Using 1.5, 1.4, we can calculate the left hand side as

$$\begin{aligned}\frac{d}{dt}\int_{X(U,t)} \rho\, u\, d\mu &= \int_U \frac{d}{dt} X^*(\rho\, u\, d\mu) = \int_{X(U,t)} \left(\frac{\partial \rho u}{\partial t} d\mu + \pounds_u(\rho u d\mu)\right) \\ &= \int_{X(U,t)} \left(u\frac{\partial \rho}{\partial t} + \rho\frac{\partial u}{\partial t} + \pounds_u(\rho)u + \rho \pounds_u(u) + \rho u \mathrm{div} u\right) d\mu\end{aligned} \tag{1.19}$$

Then we observe that

$$\begin{aligned}u(\frac{\partial \rho}{\partial t} + \pounds_u(\rho) + \rho \mathrm{div} u) &= u(\frac{\partial \rho}{\partial t} + \langle d\rho, u\rangle + \rho \mathrm{div} u) \\ &= u(\frac{\partial \rho}{\partial t} + \mathrm{div}(\rho u)) = 0\,,\end{aligned} \tag{1.20}$$

by conservation of mass. Incorporating the incompressibility condition, we have that the incompressible Euler's equations for unknown vector field, density, and pressure, u, ρ, p

respectively are given by

$$
\begin{aligned}
\frac{\partial u}{\partial t} + u \cdot \nabla u &= -\frac{1}{\rho}\nabla p\,, \\
\frac{\partial \rho}{\partial t} + u \cdot \nabla \rho &= 0\,, \\
\operatorname{div}(u) &= 0\,, \\
u(0,x) &= u_0\,,
\end{aligned}
\tag{1.21}
$$

where u_0 is the initial condition. Hereafter, we assume that the fluid is homogeneous, that is, $\rho = \rho_0 = \text{const.}$, which is absorbed into the pressure term. Although the density and velocity have evolution equations, the pressure does not. The evolution of the pressure is dictated by the divergence free condition on the velocity field. Indeed, taking the divergence of the first equation, we get

$$
-\Delta p = \operatorname{div}(u \cdot \nabla u). \tag{1.22}
$$

Thus the pressure can be obtained by solving a Poisson equation in terms of the velocity field at any given time. We will see that we need not solve for the pressure explicitly if we use the vorticity stream-formulation of Euler's equations. The equations 1.21 are not independent of the frame of reference. As we wish to utilize both the Eulerian and Lagrangian frames of reference, we seek an expression that is invariant under pull-back with the time-dependent flow induced by u. To achieve this we use the isomorphism $T_pM \cong T_p^*M$ induced by the metric tensor, since M is a Riemannian manifold. Denoting the transformation $(\cdot)^\flat : T_pM \cong T_p^*M, u \mapsto u^\flat = g^{i,j}u_j$, then the time evolution of the 1-form velocity is then given by

$$
\frac{\partial u^\flat}{\partial t} + \nabla_u u^\flat = -dp\,. \tag{1.23}
$$

Proposition 1.1. We have

$$
\pounds_u u^\flat = \nabla_u u^\flat + \frac{1}{2} d(u^\flat(u)) \tag{1.24}
$$

Proof. We will show this in coordinates, with vector components with raised indices and covectors with lowered indices. We start with

$$
\begin{aligned}
\nabla_u u^\flat + \frac{1}{2} d(u^\flat(u)) &= u^j \partial_j u_i - \Gamma_{ij}^k u_k u^j + \frac{1}{2}\partial_i(g_{kl}u^k u^l) \\
&= u^j \partial_j u_i - \frac{1}{2} u^l u^j \left(\partial_i g_{lj} + \partial_j g_{li} - \partial_l g_{ij}\right) + \frac{1}{2}\partial_i(g_{kl}u^k u^l) \\
&= u^j \partial_j u_i - \frac{1}{2} u^l u^j \left(\partial_i g_{lj} + \partial_j g_{li} - \partial_l g_{ij}\right) + \frac{1}{2}\partial_i(g_{kl}u^k u^l)\,,
\end{aligned}
\tag{1.25}
$$

and then we can use the fact that

$$\begin{aligned} &\frac{1}{2}u^l u^j\left(\partial_j g_{li}-\partial_l g_{ij}\right)=-\frac{1}{2}u^j u^l\left(\partial_l g_{ji}-\partial_j g_{il}\right)\\ &\Rightarrow \frac{1}{2}u^l u^j\left(\partial_j g_{li}-\partial_l g_{ij}\right)=0\,. \end{aligned} \tag{1.26}$$

Therefore, we obtain

$$\begin{aligned} \nabla_u u^\flat+\frac{1}{2}d(u^\flat(u)) &= u^j\partial_j u_i-\frac{1}{2}u^l u^j\partial_i g_{lj}+\frac{1}{2}\partial_i(g_{kl})u^k u^l+g_{kl}u^k\partial_j u^i\\ &= u^j\partial_j u_i+u_l\partial_j u^i=\left(\pounds_u u^\flat\right)_i\,, \end{aligned} \tag{1.27}$$

establishing the claim.

□

Using 1.1 we get that 1.23 for the 1-form velocity $\boldsymbol{u}^\flat$ can be written as

$$\frac{\partial u^\flat}{\partial t}+\mathcal{L}_u u^\flat=-d\left(p+\frac{1}{2}|u|^2\right)\,. \tag{1.28}$$

The incompressibility condition for $u^\flat$ and the definition of the divergence of a vector field 1.5 yield

$$\mathrm{div}u=0 \iff \delta u^\flat=0 \tag{1.29}$$

1.4 Vorticity-Stream Formulation

Since the fluid does not possess any internal shear forces, rotational motion within the fluid will persist over time without dissipation. Consequently, the integral of the velocity 1-form over a some closed loop, called *circulation*, in the fluid remains constant over time. This can be seen as a statement of conservation of angular momentum adapted to continuum motion. More concretely, let X be the time-dependent flow of $\boldsymbol{u}$, and denote by $C(t)\in M$ a closed contour carried along with the fluid. Then using 1.28 we infer

$$\begin{aligned} \frac{d}{dt}\int_{C(t)}u^\flat &= \int_{C_0}\frac{d}{dt}X^*\left(u^\flat\right)=\int_{C_0}X^*\left(\frac{\partial u^\flat}{\partial t}+\mathcal{L}_u u^\flat\right)\\ &= -\int_{C(t)}d\left(p+\frac{1}{2}|u|^2\right)=0\,, \end{aligned} \tag{1.30}$$

since the integral of an exact form over a closed loop is zero. Denoting by Σ, the surface enclosed by the contour C, we have that

$$\int_{C(t)}u^\flat=\int_{\Sigma(t)}du^\flat=\int_{\Sigma(t)}\tilde{\omega} \tag{1.31}$$

by Stokes' theorem, where we have defined the vorticity 2-form $\tilde{\omega}=du^\flat$. Applying conservation of circulation to 1.31 in terms of ω, we obtain

$$\frac{\partial\tilde{\omega}}{\partial t}+\mathcal{L}_u\tilde{\omega}=0\,, \tag{1.32}$$

that is, the vorticity is Lie transported by the fluid velocity. From the two-form vorticity, since M is two dimensional we can obtain a representative scalar using the Hodge-star operator, that is, $\tilde{\omega} = *\omega \in \Omega^0(M)$. Since the vorticity ω is a scalar field in two dimensions, 1.32 reduces to

$$\frac{\partial \omega}{\partial t} + u \cdot \nabla \omega = 0\,. \tag{1.33}$$

We now seek to obtain the velocity field from known vorticity. By application of the Hodge decomposition theorem [1], we have for any 1-form α on a two dimensional manifold there exists $\Phi \in \Omega^0(M), \tilde{\psi} \in \Omega^2(M)$, and $\zeta \in \Omega^1(M)$ harmonic, such that

$$\alpha = d\Phi + \delta(\tilde{\psi}) + \zeta = d\Phi - *d\psi + \zeta\,, \tag{1.34}$$

where we have associated $\tilde{\psi} = *\psi$ for $\psi \in \Omega^0(M)$ as done for the vorticity 2-form and used the identity $\delta* = - * d$. Since M is diffeomorphic to $\mathbb{S}^2$, it is simply connected and we have that the only harmonic 1-forms on M are 0 [1, 12]. Applying this to our 1-form velocity $u^\flat$, and using the metric tensor to map back onto the tangent bundle, we have that,

$$u = (u^\flat)^\sharp = (d\Phi)^\sharp - (*d\psi)^\sharp = \nabla\Phi + \nabla^\perp\psi \tag{1.35}$$

Using the incompressibility condition, we have that $\mathrm{div}(u) = \Delta\Phi = 0$. Considering $M = \mathbb{S}^2$, then we have the following claim.

Proposition 1.1. If $\Phi : \mathbb{S}^2 \to \mathbb{R}$ is harmonic, then $\Phi = c$ where $c \in \mathbb{R}$.

Proof. Using the fact that Φ is smooth, that spherical harmonics form a complete orthonormal basis for $L^2(\mathbb{S}^2)$ [66]. Furthermore, spherical harmonics $Y_\ell^m(x)$ are eigenfunctions of the Laplace-Beltrami operator on the sphere, with eigenvalues $-\ell(\ell+1)$, and we have

$$\begin{aligned} -\Delta\Phi &= \sum_{\ell=0}^{\infty} \sum_{m=-\ell}^{\ell} \hat{\Phi}_{\ell,m} \ell(\ell+1) Y_\ell^m(x) = 0 \\ &\Rightarrow \hat{\Phi}_{\ell,m} = 0 \quad \forall \ell \neq 0 \Rightarrow \Phi = \frac{1}{2}\sqrt{\frac{1}{\pi}}\,, \end{aligned} \tag{1.36}$$

□

We get that $u = \nabla^\perp\psi$ and we call ψ the *stream function*. Using the 1-form velocity again, we have

$$\omega = * * \omega = *\tilde{\omega} = *(du^\flat) = - * d(*d\psi) = -\Delta\psi\,, \tag{1.37}$$

recognizing $*d(*d) = \Delta$ as the Laplace-Beltrami operator for scalar functions on M. The solution of 1.37 will determine the stream function up to a constant, and thus we have to impose a condition on the mean. Altogether, the velocity is related to the vorticity as,

$$\begin{aligned} \omega &= -\Delta\psi, \quad \int_{\mathbb{S}^2} *\psi = 0\,, \\ u &= \nabla^{\perp}\psi\ . \end{aligned} \tag{1.38}$$

The vorticity-stream formulation allows us to obtain the solution to 1.21 by solving the following simpler system of partial differential equations

$$\begin{aligned} \frac{\partial\omega}{\partial t} + u\cdot\nabla\omega &= 0\,, \\ -\nabla^{\perp}\Delta^{-1}\omega &= u\,, \\ \mathrm{div}(u) &= 0\,, \\ u(x,0) &= u_0(x)\,. \end{aligned} \tag{1.39}$$

In forthcoming chapters we will discuss the numerical solution of 1.39. In particular, we will employ the double Fourier sphere method to the Poisson equation for the stream function with vorticity as forcing function. The transport equation for the vorticity is solved using the characteristic mapping method. In the last chapter we investigate aspects of combining both the double Fourier sphere and characteristic mapping methods to solve Euler's equations 1.21 using the vorticity-stream formulation 1.39.

Chapter 2

Double Fourier Sphere

2.1 Introduction

In this chapter we discuss the numerical solution of the Poisson equation on the two-dimensional sphere, hereafter 'the sphere', using an approximation by bivariate Fourier series. Since the sphere is a compact domain without boundary, it provides an ideal setting for function approximation using global basis functions. A natural basis for the representation of a function defined on $\mathbb{S}^2$ are spherical harmonics. These functions form a complete and orthonormal basis for $L^2(\mathbb{S}^2)$ and are eigenfunctions of the spherical Laplacian. Due to these desirable properties, fast algorithms for the spherical harmonic transform have received a significant amount of attention [51, 57, 64, 65]. However, there is an associated $\mathcal{O}(\mathrm{N}^2)$ precomputational cost inherent in these algorithms, where N is the number of grid points. Although their efficiency is applicable for many situations, for the solution of PDEs using pseudospectral methods which leverage both the spectral and spatial representations of the function, this can set limitations on the use of adaptive discretizations and on practical solution times at high resolutions. We instead consider an alternative approach using a bivariate Fourier series representation of a function on the sphere.

The double Fourier sphere utilizes an extension of the standard spherical coordinate system defined by the coordinates $(\lambda, \theta) \in [-\pi, \pi] \times [0, \pi]$, where λ is the azimuthal angle, and θ is the polar angle. The extension results in a function that is 2π-periodic in both directions, lending to its representation as a bivariate Fourier series. The forward and inverse transforms can then be performed with $\mathcal{O}(\mathrm{N} \log \mathrm{N})$ operations using existing highly optimized algorithms [14, 22] , making the implementation relatively simple and parallelizable.

We present a review of the double Fourier sphere technique, its algorithmic imple-

mentation and numerical tests for the solution of the Poisson equation on the sphere. As an additional test of the capabilities of our implementation, we also consider the solution of the heat and Allen-Cahn equations on the sphere.

2.2 Double Fourier sphere method

A doubly periodic representation of a function on the sphere can be achieved by stacking the standard spherical coordinate map with a reflected version over one of the poles which is then translated (rotated) by π along the azimuth. An example of this mapping is given in figure 2.1. Denote by $\mathbb{S}^2$ the boundary of the unit ball in $\mathbb{R}^3$ using the regular Euclidean metric. Let $x \in \mathbb{R}^3$ with $||x|| = 1$, be parameterized using the standard spherical coordinate system where $(\lambda, \theta) \in [-\pi, \pi] \times [0, \pi]$ are the azimuthal and polar angles such that $\theta = 0$ is the 'north pole' at the point $(x, y, z) = (0, 0, 1)$. We note that in this domain the map $\varphi^{-1} : [-\pi, \pi] \times [0, \pi] \to \mathbb{S}^2$ is not a bijection since at the poles, all azimuthal angles correspond to the same point. Nevertheless, consider the function $u \circ \varphi^{-1} : [-\pi, \pi] \times [0, \pi] \to \mathbb{R}$. Tts doubly periodic extension, denoted by $\tilde{u}$ is given as:

$$\tilde{u}(\lambda, \theta) = \begin{cases} u(\lambda, \theta) & \text{for } (\lambda, \theta) \in [-\pi, \pi] \times [0, \pi]\,, \\ u(\lambda + \pi, -\theta) & \text{for } (\lambda, \theta) \in [-\pi, 0] \times [\pi, 0]\,, \\ u(\lambda - \pi, -\theta) & \text{for } (\lambda, \theta) \in [0, \pi] \times [-\pi, 0]\,. \end{cases} \tag{2.1}$$

The resulting extended function is now doubly periodic in both directions and single valued at the poles. The original function can then be recovered via restriction of $\tilde{u}(\lambda, \theta)$ to $(\lambda, \theta) \in [-\pi, \pi] \times [0, \pi]$. Consider now a uniform partition of the extended domain, corresponding to two regular latitude-longitude grids on the sphere, with grid points (λ_p, θ_q) defined by,

$$\lambda_q = -\pi + (q-1)\frac{2\pi}{n},\ 1 \le q \le n,\ \ \theta_p = -\pi + (p-1)\frac{2\pi}{m},\ 1 \le p \le m. \tag{2.2}$$

A uniformly sampled function on this grid admits a bivariate Fourier series of the form

$$\tilde{u}(\lambda, \theta) \approx \sum_{j=-m/2}^{m/2} \sum_{k=-n/2}^{n/2} \hat{u}_{jk} e^{ij\theta} e^{ik\lambda}\,, \tag{2.3}$$

with the corresponding Fourier coefficients defined by

$$\hat{u}_{jk} = \frac{1}{nm} \sum_{p=1}^{m} \sum_{q=1}^{n} \tilde{u}(\lambda, \theta) e^{-ij\theta_p} e^{-ik\lambda_q}. \tag{2.4}$$

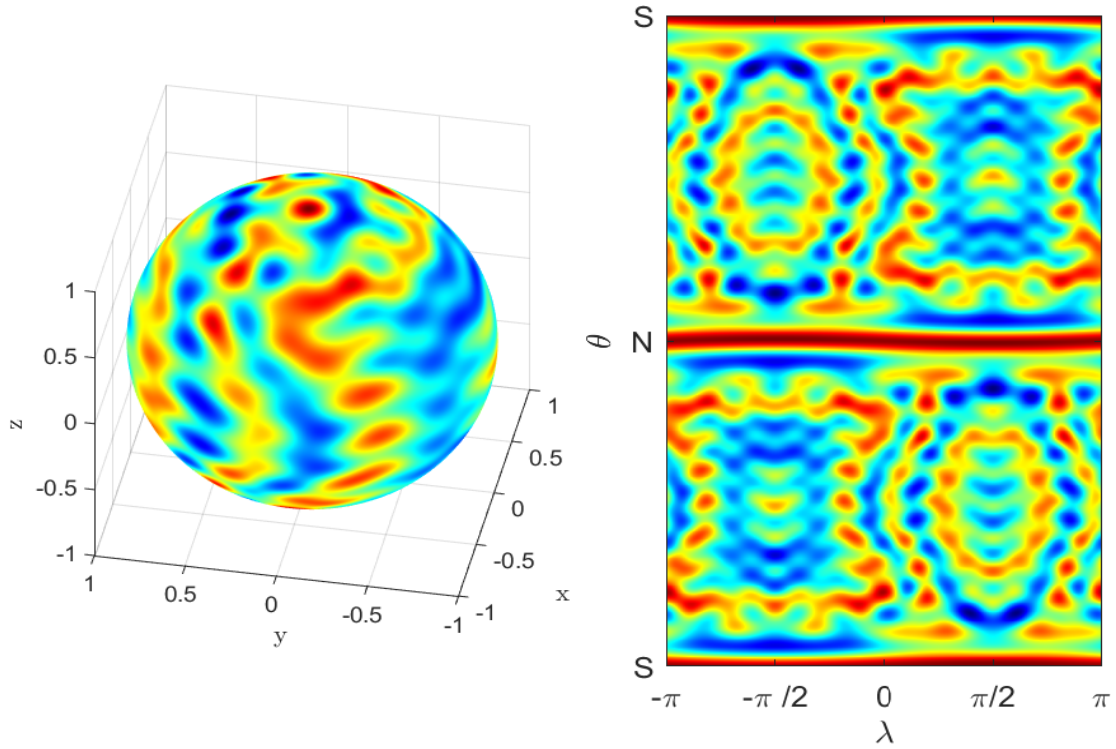

Figure 2.1: Depiction of the mapping given by (2.1) for a function on the sphere. Each pole is associated with a single point.

We note that since each pole is represented as an entire line in this extended domain, not all smooth functions on this extended domain will correspond to a smooth function on the sphere [63]. This correspondence can be ensured by requiring that $\tilde{u}(\lambda, 0) = u_N$ and $\tilde{u}(\lambda, -\pi) = \tilde{u}(\lambda, \pi) = u_S \ \forall \lambda \in [-\pi, \pi]$ where $u_N, u_S \in \mathbb{R}$. Note that

$$\begin{aligned} \tilde{u}(\lambda, \pm\pi) &= \sum_{j=-m/2}^{m/2} \sum_{k=-n/2}^{n/2} \hat{u}_{jk} e^{\pm i\pi j} e^{ik\lambda} \\ &= \sum_{j=-m/2}^{m/2} \sum_{k=-n/2}^{n/2} \hat{u}_{jk} (-1)^j e^{ik\lambda} \\ &= \sum_{\substack{k=-n/2 \\ k\neq 0}}^{n/2} e^{ik\lambda} \sum_{j=-m/2}^{m/2} (-1)^j \hat{u}_{jk} + \sum_{j=-m/2}^{m/2} (-1)^j \hat{u}_{j0}. \end{aligned} \tag{2.5}$$

Since the second sum is a constant, independent of λ, we obtain the condition

$$\sum_{j=-m/2}^{m/2} (-1)^j \hat{u}_{j,k} = 0, \ |k| \geq 1. \tag{2.6}$$

ensuring that the function is single valued at the south pole. Similarly, the condition at the north pole is given by,

$$\sum_{j=-m/2}^{m/2} \hat{u}_{j,k} = 0, \ |k| \geq 1. \tag{2.7}$$

Together these two conditions form the *pole conditions* for a function represented in the form 2.3. We note that the pole conditions are not explicitly enforced in the method and thus instead provide a means of evaluation of our numerics.

The use of this approach has seen many different iterations before arriving at this most recent form as given in [38]. The origin of the bivariate Fourier series for spectral analysis on the sphere comes from the work of Merilees [37] and was also developed and studied by Orzag [46] around the same time. A form of the method, as proposed by Orzag, which was further expanded upon by Yee in [73], uses an expansion of the form

$$u(\lambda,\theta) = \sum_{m=-\infty}^{\infty} \sum_{\ell=0}^{\infty} \hat{u}_{\ell,m} e^{-im\lambda} \left[(1-s)\cos(\ell\theta) + s\sin(\ell\theta)\right] , \tag{2.8}$$

where the spectral coefficients are given by

$$\hat{u}_{\ell,m} = \begin{cases} \dfrac{c}{4\pi^2} \displaystyle\int_0^{\pi}\int_{\pi}^{\pi} u(\lambda,\theta) e^{im\lambda} \cos(\ell\theta)\, d\lambda d\theta & \text{for } m \text{ even}\,, \\ \dfrac{c}{4\pi^2} \displaystyle\int_0^{\pi}\int_{\pi}^{\pi} u(\lambda,\theta) e^{im\lambda} \sin(\ell\theta) d\lambda d\theta & \text{for } m \text{ odd}\,. \end{cases} \tag{2.9}$$

for $c = 1$ if $\ell = 0$ and $c = 2$ otherwise. As outlined in [13], basis functions of this form were not seen as suitable to solve advection equations on the sphere since it was necessary to impose a constraint on the even latitudinal wavenumbers, in order to satisfy the pole conditions. Furthermore, these functions do not avoid the singularity that can arise in the numerical solution of Poisson's equation on the sphere, as we will see in the following section. This necessitates the use of an interior grid that does not include the poles. To remedy the need for such constraints, Cheong [13] proposed to use basis functions that satisfy the pole conditions inherently. The expansion is given by

$$u(\lambda,\theta) = \sum_{k=-n/2}^{n/2} u_j(\theta) e^{ik\lambda} , \tag{2.10}$$

for the coefficients function,

$$\begin{cases} u_0(\theta) &= \displaystyle\sum_{k=0}^{N-1} \hat{u}_{j,0} \cos(k\theta) \text{ for } j = 0\,, \\ u_j(\theta) &= \displaystyle\sum_{k=0}^{N-1} \hat{u}_{j,k} \sin(k\theta) \text{ for odd } j\,, \\ u_j(\theta) &= \displaystyle\sum_{k=0}^{N-1} \hat{u}_{j,k} \sin(\theta)\sin(k\theta) \text{ for } j \text{ even } (\neq 0)\,, \end{cases} \tag{2.11}$$

and the spectral coefficients are given by

$$
\begin{cases}
\hat{u}_{j,k} &= \dfrac{b}{N}\displaystyle\sum_{p=0}^{N-1} u_j(\theta_p)\cos(k\theta_p/N) \text{ for } j=0\,, \\
\hat{u}_{j,k} &= \dfrac{c}{N}\displaystyle\sum_{p=0}^{N-1} u_j(\theta_p)\sin(k\theta_p/N) \text{ for odd } j\,, \\
\hat{u}_{j,k} &= \dfrac{c}{N}\displaystyle\sum_{p=0}^{N-1} (u_j(\theta_p)/\sin(\theta_p))\sin(k\theta_p/N) \text{ for } j \text{ even } (\neq 0)\,,
\end{cases}
\tag{2.12}
$$

where $b = 1$ for $j = 0$ and $b = 2$ otherwise, $c = 1$ for $j = N$ and $c = 2$ otherwise. When solving the spherical Poisson equation using these basis functions, the use of interior grids is still necessary. Furthermore, for both of these representations, the solution requires the solution of multiple algebraic equations which depend on the the parity of the wavenumbers. We found that the method given by [38] provided a more simplistic approach for solving the spherical Poisson equation while imposing the least amount of constraints on the solution procedure and computational domain.

2.3 Numerical Implementation

In this section we outline the numerical implementation of the double Fourier sphere method for the solution of partial differential equations on the sphere. In particular, we demonstrate that issues related to the defining differential operators in the spherical coordinate system can be alleviated by considering the discretized differential operators as acting on the coefficient space. It is well known that operations in the standard spherical coordinate system, such as differentiation in the azimuthal direction, suffer from coordinate singularities at the poles. Issues pertaining to these singularities at the poles are broadly referred to as the 'pole-problem'. Many of these problems arise from the necessity of evaluating trigonometric terms arising in differential operators defined in this coordinate system. We demonstrate how the use of a algebraic representations of the necessary differential operators on the space of coefficients lead to bounded and well-defined expression. Where many analytic representations of certain operators in physical space suffer from coordinate singularities, their algebraic representation in the coefficient space does not.

2.3.1 Operations in Frequency Space

Issues related to the use of the spherical coordinate system, such as the oversampling of grid points near the poles and the inherent coordinate singularity are broadly referred

to as the 'pole-problem'. Numerous methods for addressing this problem have been presented and analyzed in the past five decades, cf. [7,16,56,68,69] and references therein. The inevitability of computational issues in the numerical solution of a PDE on the sphere when using a regular latitude-longitude coordinate system is undisputed. Though the cause is still the same, often the remedy of an issue related to the pole will be problem specific.

Although the issues related to use of rectangular grids in the spherical coordinate parametric space may be aplenty, there are still many desirable properties. For our purposes, these are a simple data structure facilitating optimally local, tensor-product interpolation techniques and the fact that we can obtain a uniform grid in the (λ, θ) parametric space. The latter of which allows for the use of the discrete fast Fourier transform. Furthermore, when represented as a bivariate Fourier series, many issues related to differentiating a function in spherical coordinates can be alleviated. We explain this fact by way of an example, considering the spherical Poisson equation

$$\Delta u = u_{\theta\theta} + \frac{\cos(\theta)\sin(\theta)}{\sin^2(\theta)} u_\theta + \frac{1}{\sin^2(\theta)} u_{\phi\phi} = f\,, \tag{2.13}$$

for some forcing function $f : \mathbb{S}^2 \to \mathbb{R}$. In the standard spherical coordinate system, and in the extended one we have defined, the spherical Poisson operator has a coordinate singularity at the poles. Using the trigonometric multiplication matrices defined in Appendix A, the discrete Laplace operator, $\mathbf{L}$, can be expressed using the Kronecker product,

$$\mathbf{L} = \mathbf{I}_n \otimes (\mathbf{D}_m^{(2)} + \mathbf{T}_{\sin^2}^{-1} \mathbf{T}_{\cos\sin} \mathbf{D}_m) + \mathbf{D}_n^{(2)} \otimes \mathbf{T}_{\sin^2}^{-1}. \tag{2.14}$$

The resultant discrete spherical Laplace operator is a block diagonal matrix whose individual blocks are non-singular. Each block possesses a sparsity pattern which admits a linear-cost inversion. As previously noted, in order to obtain a unique solution, we must also impose a condition on the mean of the function. The constant shift that can appear in the solution of (2.13) manifests itself as a non-zero dimension of the nullspace for the $n/2 + 1$ block of $\mathbf{L}$, corresponding to the wavenumber $n = 0$. This can be remedied by

replacing the $m/2+1$ row of this block by the discretized mean, given by

$$\begin{aligned}
\iint_{\mathbb{S}^2} u(\lambda,\theta)\sin(\theta)\mathrm{d}\lambda\mathrm{d}\theta &\approx \sum_{\mathrm{j}=-\mathrm{m}/2}^{\mathrm{m}/2}\sum_{\mathrm{k}=-\mathrm{n}/2}^{\mathrm{n}/2}\hat{\mathrm{u}}_{\mathrm{jk}}\int_0^{\pi}\sin(\theta)\mathrm{e}^{\mathrm{ij}\theta}\mathrm{d}\theta\int_{-\pi}^{\pi}\mathrm{e}^{\mathrm{ik}\lambda}\mathrm{d}\lambda \\
&= 2\pi\sum_{j=-m/2}^{m/2}\hat{u}_{jk}\int_0^{\pi}\sin(\theta)e^{ij\theta}\mathrm{d}\theta + 2\sum_{\mathrm{j}=-\mathrm{m}/2}^{\mathrm{m}/2}\sum_{\mathrm{k}=-\mathrm{n}/2}^{\mathrm{n}/2}\hat{\mathrm{u}}_{\mathrm{jk}}\frac{\sin(\mathrm{k}\pi)}{\mathrm{k}}\int_0^{\pi}\sin(\theta)\mathrm{e}^{\mathrm{ij}\theta}\mathrm{d}\theta \\
&= 2\pi\sum_{j=-m/2}^{m/2}\hat{u}_{jk}\frac{1}{2i}\left(\frac{e^{i\pi(j+1)}-1}{i(j+1)}-\frac{e^{i\pi(j-1)}-1}{i(j-1)}\right) = 2\pi\sum_{j=-m/2}^{m/2}\hat{u}_{j0}\frac{1+e^{ij\pi}}{1-j^2} = 0\,.
\end{aligned} \tag{2.15}$$

2.4 Numerical Tests

In this section we provide tests of the implementation for the solution of some particular partial differential equations on the sphere. We begin by testing the method to solve the Poisson equation for various forcing functions containing different scales. Though this was the primary intention of developing an implementation of the double Fourier sphere method as a means of obtaining the stream function from the vorticity, we additionally consider the solution of the Heat and Allen-Cahn equations. For these equations, a spatial discretization using a Fourier series results in a system of stiff ordinary differential equations in the coefficients. Since the discrete Laplace operator present in both these equations admits linear cost inversion, implicit time-marching method can be implemented efficiently. These supplementary results serve to test the flexibility of the implementation and indicate some other possible future directions of investigation.

In order to assess the accuracy of the numerical implementation, we evaluate the error in the numerical solution compared to the known analytic one in the norms

$$\begin{aligned}
\|f(\lambda_i,\theta_j,t)\|_{\ell^\infty(\Omega)} &= \max_{i,j}\{|f(\lambda_i,\theta_j,t)|\}\,, \\
\|f(\lambda_i,\theta_j,t)\|_{\ell^2(\Omega)} &= \left(\sum_i^N\sum_j^N f(\lambda_i,\theta_j,t)^2\Delta\lambda\Delta\theta\sin(\theta_j)\right)^{1/2},
\end{aligned} \tag{2.16}$$

where $\Delta\lambda, \Delta\theta$ are the grid spacings in the azimuthal and polar directions respectively and (λ_i,θ_j) for $i,j=1,\ldots,N$ are the grid points within the computational domain. Furthermore, to assess if the numerical solution remains single-valued at the poles, we calculate the error in the pole condition as

$$P = \max\left\{\max_{k\neq 0}\left(\left|\sum_{j=-m/2}^{m/2}\hat{u}_{j,k}\right|\right), \max_{k\neq 0}\left(\left|\sum_{j=-m/2}^{m/2}(-1)^j\hat{u}_{j,k}\right|\right)\right\}. \tag{2.17}$$

2.4.1 Poisson Equation

We consider the family of forcing functions in the form

$$f(\lambda,\theta) = \ell(\ell+1)\sin^{\ell}(\theta)\cos(\ell\lambda) + (\ell+1)(\ell+2)\cos(\theta)\sin^{\ell}(\theta)\cos(\ell\lambda). \tag{2.18}$$

The resulting exact solution of (2.13) is given by

$$u_{exact}(\lambda,\theta) = -\sin^{\ell}(\theta)\cos(\ell\lambda) - \cos(\theta)\sin^{\ell}(\theta)\cos(\ell\lambda) \tag{2.19}$$

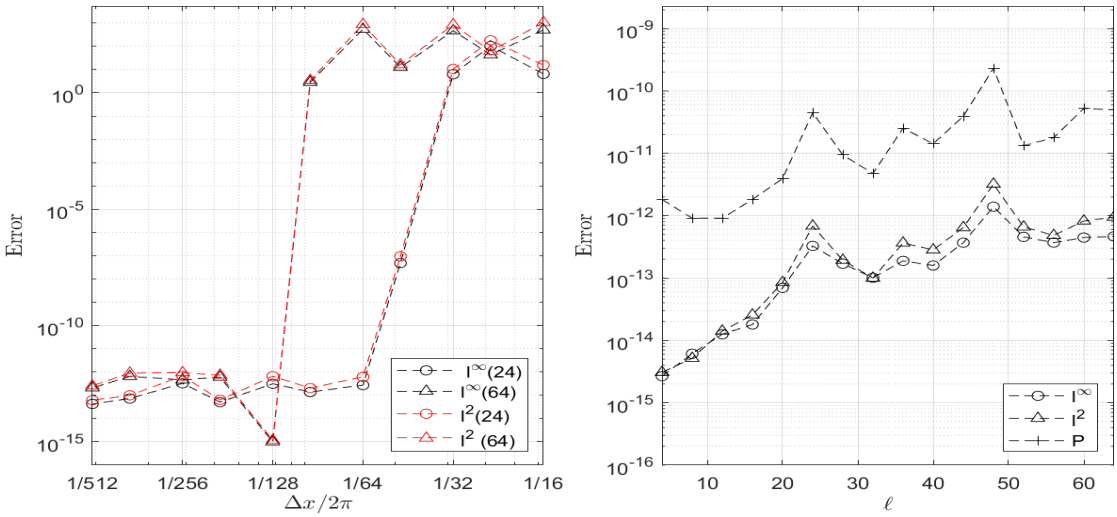

Figure 2.2: Left: Convergence plots in both norms for a forcing function with $\ell = 24, 64$. Right: Error in both norms and the pole condition for various values of ℓ from 4 to 64. The error was computed on an equally spaced grid of size $2\pi/256$.

It was found that our numerics agreed very well for the error but were approximately on the $\mathcal{O}(10^5)$ higher in the values of the pole condition for all values of ℓ than those reported in [38]. We deem this is due to round-off error, as their values reported are lower than the machine precision for which these calculations were performed.

2.4.2 Heat Equation

It was found in [46], that time marching methods using the half-range cosine and sine series converged to the incorrect solution if the pole conditions were not imposed explicitly. We provide a brief investigation of the capabilities of our implementation to perform time-stepping. For the numerical solution of the heat equation, we consider a second-order Crank-Nicolson time-stepping method, given by,

$$\frac{u^{n+1} - u^{n}}{\Delta t} = \frac{1}{2}\left(Lu^{n+1} + Lu^{n}\right) \tag{2.20}$$

where L is given by 2.14. The numerical test we consider, is the heat equation with a simplifying thermal diffusivity. Namely, we consider

$$u_t = \frac{1}{\ell(\ell+1)}\Delta u \ , \quad u(0,\lambda,\theta) = Y_\ell^m(\lambda,\theta)\,, \tag{2.21}$$

whose exact solution is given by

$$u(t,\lambda,\theta) = e^{-t}Y_\ell^m(\lambda,\theta). \tag{2.22}$$

The results of the numerical test are depicted in 2.3. It was found that the implementation produces the expected second-order accuracy globally in time and the pole condition was satisfied to high accuracy for all step sizes.

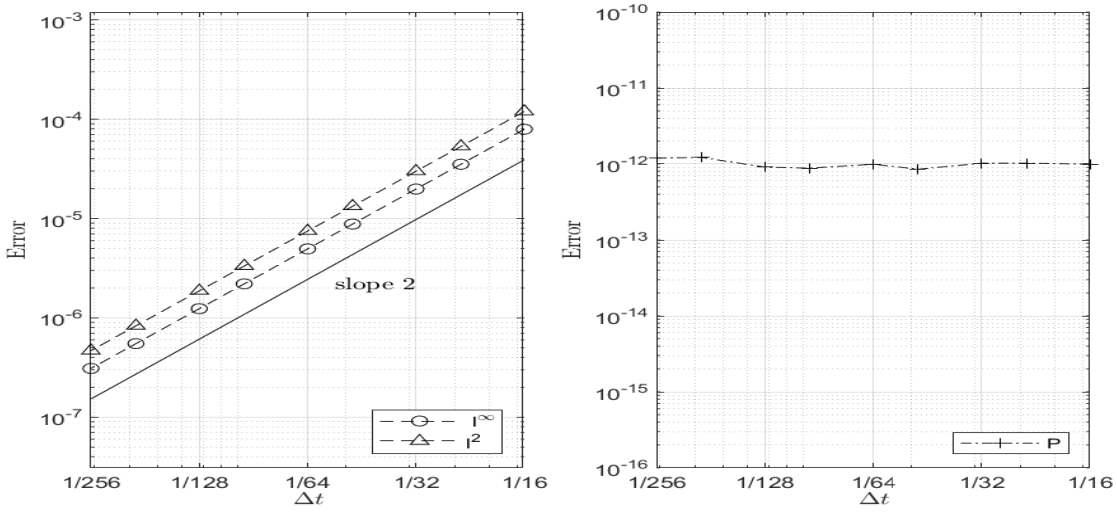

Figure 2.3: Left : Convergence in time plots in both norms. Right: Pole condition. The error was computed on a spatial grid of 128×128 points.

2.4.3 Allen-Cahn Equation

The Allen-Cahn equation is a non-linear reaction-diffusion equation, first derived as describing phase separation in iron alloys [4]. The equation is given by

$$u_t = \epsilon\Delta u + u - u^3\,, \tag{2.23}$$

where $\epsilon << 1$ is a constant. The non-linearity is the result of a double-well potential and solutions exhibit equilibria for $u = \pm 1$. We consider a first-order in time operator splitting scheme as a time-marching method [32]. We first compute an intermediate solution, v, to the heat equation with thermal diffusivity ϵ and then solve the ordinary differential equation

$$\frac{dv}{dt} = v - v^3, \quad v(0) = v_0\,, \tag{2.24}$$

whose analytic solution is given by

$$v(t) = \frac{v_0}{\sqrt{e^{-2t} - v_0^2(e^{-2t} - 1)}}\,. \tag{2.25}$$

If we compute the intermediate solution using an implicit Euler step, the time-marching scheme is given by

$$\begin{aligned} v &= (I - \epsilon \Delta t L)^{-1} u^n\,, \\ u^{n+1} &= \frac{v}{\sqrt{e^{-2t} - v^2(e^{-2t} - 1)}}\,. \end{aligned} \tag{2.26}$$

As initial condition we consider the following function from [38]:

$$u_0(\lambda, \theta) = \cos(\cosh(5\sin(\theta)\cos(\theta)\cos(\lambda)) - 10\sin(\theta)\sin(\lambda))\,. \tag{2.27}$$

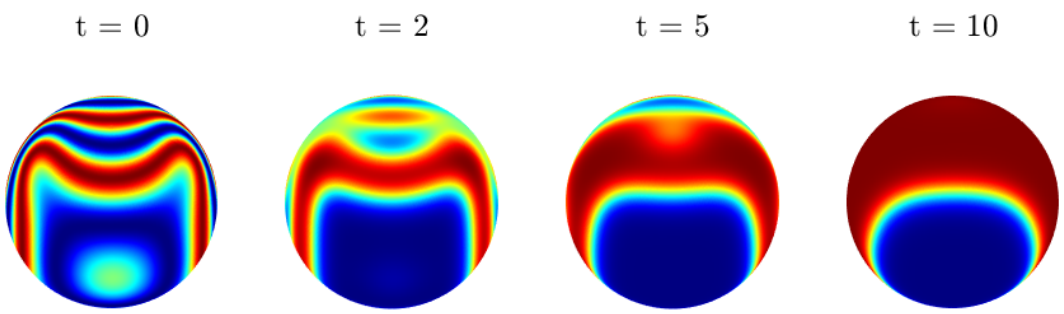

Figure 2.4: Depiction of the solution of the Allen-Cahn equation at times $t = 0, 2, 5, 10$.

The numerical solution exhibits the stable equilibria expected analytically. The ability of our implementation to perform time-stepping for partial differential equations whose resulting ordinary differential equations in coefficient space offers a promising direction of research. An analysis of other algorithms to perform time-stepping on the Fourier coefficients in highly-oscillatory systems could be an interesting avenue to explore. Further numerical experiments and analysis of the method in its present form are warranted and the subject of current research.

Chapter 3

The Characteristic Mapping Method for Linear Transport on a Sphere

3.1 Background

The numerical solution of the transport equation on the sphere plays an essential role in many geophysical applications. For example, the advection of a scalar field such as temperature or chemical concentration on the globe is fundamental to global atmospheric modeling. The efficient transport of quantities containing multiple scales or with poor regularity remains a challenge. In the context of tracer species transport, multiple quantities are advected over long periods of time, carrying inherently subgrid information with them [62]. Computational costs associated with these simulations at high resolutions can often be limiting [49].

The evolution of the advected quantity may be viewed from either the Eulerian or Lagrangian perspectives. Often, numerical methods for the solution of the advection equation will take a hybrid approach, leveraging the added benefits of both of these frameworks. In the Eulerian framework the relevant quantities are discretized on a static grid, allowing for ease of access to the solution and an easily parallelizable implementation. Without the use of highly refined meshes, sub-grid features in the solution can be lost, resulting in numerical dissipation. In order to avoid the added computational cost due to uniform mesh refinement, adaptive techniques can be used to resolve finer features [8, 21]. Furthermore, Eulerian schemes suffer from restrictive time-stepping constraints imposed by the Courant-Friedrichs-Levy condition. Lagrangian schemes alleviate these constraints

by considering grid points which follow particles trajectories in the flow. The resulting solutions are generally less prone to numerical dissipation and have better stability properties [58]. A well-known difficulty arising in these schemes is that a well-ordered set of grid points will become increasingly disordered over time [48, 67]. This can lead to sampling issues for the evolution of the advected quantity. To overcome this difficulty the use of frequent remapping or remeshing steps is often needed. One approach to avoid excessive mesh distortion is to consider a remeshing step at regular time intervals, such as in [5, 6, 35, 45]. In practice, remeshing can be computed directly by introducing a new set of ordered particles on the mesh and interpolating from the previous trajectories. Another, more recent approach, considers interpolating the inverse flow-map for the Lagrangian trajectories and then resampling the initial advected quantity [9–11].

The semi-Lagrangian (SL) approach is to maintain the representation of the advected quantity on a fixed Eulerian grid while discretizing the evolution from the Lagrangian frame. Related approaches include the Arbitrary Lagrangian-Eulerian method [27], particle-mesh methods [15], and more recent hybrid schemes [28, 54, 72]. There are also conservative SL frameworks, which have seen successful application for transport on the sphere [26, 30]. Level-set methods offer another popular SL scheme for the linear advection of sets and surfaces [47]. In these methods, characteristics are traced back in time and the advected quantity is updated via interpolation on an Eulerian grid. Higher order accuracy can be generated within the level-set framework by additionally transporting gradient information of the solution [44, 53]. For quantities containing sub-grid features or for sets with poor regularity, the transport of gradient information is infeasible. Recently, this problem was addressed by Mercier et al. [36] for the linear transport of arbitrary sets in a two and three dimensional periodic domain. This method is based on the work of Kohno and Nave [29] and has recently been applied for the two-dimensional incompressible Euler equations by Yin et al. [74]. In this chapter, these insights are applied for linear advection in a two dimensional spherical geometry.

We present an implementation of the Characteristic Mapping (CM) method for the numerical solution of the linear transport equation on the two-dimensional sphere. For the linear transport equation, the flow map generated by the advecting velocity field and the definition of the initial condition contain all information needed for its solution. The CM method dissociates these two quantities by considering the numerical quantity of interest in the advection scheme to be the flow map itself. Analytically, the map satisfies a vector valued advection equation for the same velocity field. Its solution yields

a function which maps a given arrival point along the characteristics back in time t, to its departure point. The map itself possesses a semigroup structure which facilitates its own evolution via composition. Numerically, we leverage this property using the built-in interpolation structure of the Gradient-Augmented Level Set (GALS) method [44]. Due to the resulting functional definition the evolution of the advected quantity is then readily given by the pullback of the initial condition by the numerically computed map, thus avoiding the necessity to ever be discretized.

Once computed, the backward characteristic map for a given velocity field allows for the evolution of multiple quantities simultaneously via composition. The accurate tracking of the locations of these quantities is determined by the accuracy for which the map is computed. Nevertheless, since the initial condition is never discretized, the method possesses the capability of transporting arbitrarily fine features via simple evaluation with the map. As a result, the method is able to attain exponential resolution in linear computation time.

This chapter is organized as follows. We begin with the mathematical formulation of the CM method for the solution of the linear advection equation on the two-dimensional sphere. Thereafter, we describe the numerical implementation, outlining the spatial discretization via Hermite cubic interpolation along with the time evolution using the GALS method. We then present numerical tests of the method for four standard test cases involving a variety of flow environments, as given in [42]. Finally, we conclude with a presentation of the unique features of the method by a 'zoom-in' on the solution for the transport of a multi-scale function and a fractal set in a complex flow environment.

3.2 Mathematical Framework

In this section we outline the mathematical framework for the CM method for linear advection on the two dimensional sphere. We seek the evolution of a time-dependent scalar field $\phi : \mathbb{S}^2 \times \mathbb{R} \to \mathbb{R}$, whose evolution is dictated by a known time-dependent velocity field, $u : \mathbb{S}^2 \times \mathbb{R} \to T\mathbb{S}^2$. We will denote $x \cdot y = g(x, y)$ where $g = \langle \cdot, \cdot \rangle : T\mathbb{S}^2 \times T\mathbb{S}^2 \to \mathbb{R}$ is the standard Riemannian metric on the 2-sphere. Let $\gamma(t)$ be an integral curve of u. The advection equation in strong form is given by

$$\frac{d}{dt}\phi(\gamma(t), t) = \partial_t \phi + u(\gamma(t), t) \cdot \nabla_{\mathbb{S}^2} \phi(\gamma(t), t) = 0, \quad \phi(\boldsymbol{x}, 0) = \phi_0(\boldsymbol{x})\,. \tag{3.1}$$

Here the gradient at $p \in \mathbb{S}^2$ is given by

$$\nabla_p \phi = g^{i,j} \partial_j \phi \tag{3.2}$$

Since $\mathbb{S}^2$ is a Riemannian manifold, we express the volume form in local coordinates (x_1, x_2) as $d\mu = \sqrt{|g|}dx^1 \wedge dx^2$. Let $X : \mathbb{S}^2 \times \mathbb{R} \to \mathbb{S}^2$ be the time-dependent flow map of the velocity field and let $U_0 \subseteq M$ be a fixed reference configuration in the fluid domain. From the Transport Theorem 1.1 of Chapter 1, and noting that X has a smooth inverse, we deduce that

$$\begin{aligned} &\frac{d}{dt}\int_{X(U_0,t)} \phi \, d\mu = 0 \\ &\Rightarrow \int_{X(U_0,t)} \phi(x,t)\, d\mu = \int_{U_0} \phi(x,0) d\mu \\ &= \int_{X(U_0,t)} X^{-1*}\left(\phi(x,0)d\mu\right) = \int_{X(U_0,t)} \phi_0 \circ X^{-1} \det\left(\nabla X^{-1}\right) d\mu \,. \end{aligned} \tag{3.3}$$

Since U_0 is arbitrary and ϕ is well-defined everywhere in $\mathbb{S}^2$, we obtain the solution to 3.1 as

$$\phi(x,t) = \phi(\boldsymbol{X}^{-1}(x,t),0)\det\left(\nabla \boldsymbol{X}^{-1}(x,t)\right). \tag{3.4}$$

We see explicitly that the evolution of ϕ is determined its initial condition and the inverse of the flow map $\boldsymbol{X}^{-1}$, called the *backward characteristic map*, generated by the advecting velocity field. The CM method leverages this insight by considering the numerical quantity of interest to be the inverse flow map $\boldsymbol{X}^{-1}$ rather than the advected quantity ϕ. Due to the definition of the flow map, we have that along the integral curves $\gamma(t)$ of $\boldsymbol{u}$,

$$\boldsymbol{X}^{-1}(\gamma(t),t) = \boldsymbol{\gamma}(0). \tag{3.5}$$

Taking the total derivative with respect to time of 3.5, we see that $\boldsymbol{X}^{-1}$ also satisfies a vector-valued advection equation for the same velocity field where the initial condition is the identity map, i.e.,

$$\begin{aligned} &\frac{d}{dt}\boldsymbol{X}^{-1} = \partial_t \boldsymbol{X}^{-1} + \nabla_u \boldsymbol{X}^{-1} = 0\,, \\ &X_0^{-1} = \mathrm{id}_{\mathbb{S}^2}\,. \end{aligned} \tag{3.6}$$

The semigroup structure of the flow map, and its inverse, discussed in Chapter 1, facilitates the evolution of the flow map via composition. Indeed, if we consider a partition of the time interval into m subdivisions $[\tau_i, \tau_{i+1}] \subset [0,T]$ for $i \in \{0,1,\ldots,m-1\}$, where T is some final integration time, then we can consider the evolution of the backward characteristic map, denoted in each subinterval by $\boldsymbol{X}_{[\tau_{i+1},\tau_i]}$, as the solution to

$$\begin{aligned} &\partial_t \boldsymbol{X}_{[\tau_{i+1},\tau_i]} + \langle u, \nabla_{\mathbb{S}^2} \boldsymbol{X}_{[\tau_{i+1},\tau_i]} \rangle = 0 \quad \text{for } t \in [\tau_i, \tau_{i+1}]\,, \\ &\boldsymbol{X}_{[\tau_{i+1},\tau_i]}(\boldsymbol{x}, t_i) = \boldsymbol{x}\,. \end{aligned} \tag{3.7}$$

Using the semigroup property of the flow, we obtain the global solution operator by composition of each sub-map, that is,

$$\boldsymbol{X}_{[t,0]}(\boldsymbol{x},t) = \boldsymbol{X}_{[\tau_1,0]} \circ \boldsymbol{X}_{[\tau_1,\tau_2]} \cdots \circ \boldsymbol{X}_{[t,\tau_m]}(\boldsymbol{x},t). \tag{3.8}$$

We note that this property of the backward characteristic map is independent of the partition, and thus allows for the adaptive decomposition of the flow in time.

Since the solution to 3.6 is independent of the solution to 3.1, the method does not depend on the initial condition, i.e., 3.4 holds for all initial conditions $\phi_0(\boldsymbol{x})$ that are well-defined on the domain. The regularity or even the definition of the initial condition thus bears no constraint on its transport. This opens the possibility of advecting multiple quantities, arbitrary sets, and even fractal ones, with the use of a single backward characteristic map for a given flow.

3.2.1 Computational domain

In congruence with the computational domain taken for the solution of the stream function, we compute the solution on the "doubled-up" regular latitude-longitude coordinate system used in Chapter 2. We recall, the extended solution $\tilde{\phi}$, resulting from the transformation 2.1, should be 2π-periodic in both directions and single-valued along each pole. The true solution ϕ can be recovered via restriction to $(\lambda,\theta) \in [-\pi,\pi] \times [0,\pi]$. If ϕ is a solution to 3.1 then its extension solves

$$\partial_t \tilde{\phi} + \nabla_{\tilde{u}} \tilde{\phi} = 0, \quad \tilde{\phi}(x,0) = \tilde{\phi}_0(x)\,, \tag{3.9}$$

where $\tilde{u} = (\tilde{u}_\lambda, \tilde{u}_\theta)^T$ is the extension of the advecting velocity given by

$$\tilde{u}(\lambda,\theta) = \begin{cases} (u_\lambda(\lambda,\theta), u_\theta(\lambda,\theta))^T & \text{for } (\lambda,\theta) \in [-\pi,\pi] \times [0,\pi]\,, \\ (u_\lambda(\lambda+\pi,-\theta), -u_\theta(\lambda+\pi,-\theta))^T & \text{for } (\lambda,\theta) \in [-\pi,0] \times [-\pi,0]\,, \\ (u_\lambda(\lambda-\pi,-\theta), -u_\theta(\lambda-\pi,-\theta))^T & \text{for } (\lambda,\theta) \in [0,\pi] \times [-\pi,0]\,, \end{cases} \tag{3.10}$$

resulting in a consistent solution on both coordinate charts of the sphere. The necessity of the transformation 3.10 can be understood by considering the transformation as applied to the Helmholtz-Hodge decomposition of a vector field tangent to the surface of the sphere. We write the vector field, u, as the sum

$$u = \nabla_{\mathbb{S}^2} f + \hat{n} \times \nabla_{\mathbb{S}^2} \psi\,, \tag{3.11}$$

where $\hat{n}$ is the unit normal to the sphere and $f, \psi : \mathbb{S}^2 \to \mathbb{R}$. The transformed velocity $\tilde{u}$ is obtained by first applying the extension of f and ψ in the spherical coordinate system then taking the gradient and surface curl respectively of each transformed function. Were u to be irrotational, then the transformation 3.10 follows readily from application of the chain rule to the transformed potential $\tilde{f}$. In the case that u is solenoidal, the transformation follows from application of the chain rule on the extended domain and the fact that the orientation changes. Thus, although the component $\nabla\tilde{\psi}$ is rotated by $\pi/2$, the unit normal acquires an additional minus sign, resulting in a consistent transformation to the case when the field is irrotational.

Since the stream function is obtained as the solution of the Poisson equation with vorticity as forcing function using the double Fourier sphere method, we find it advantageous to also phrase the advection part of the solution strategy on this extended domain. Although, we will see how issues related to the coordinate system limit the scope of velocity fields we may consider. In the following chapter we address this issue and offer possible solutions. The use of the extended domain also facilitates a tensor-product interpolation approach used in the Gradient-Augmented Level Set (GALS) method to solve the linear advection equation.

3.3 Numerical Framework

In this section we present the numerical framework for the GALS and CM methods. We begin with a description of the spatial discretization using Hermite cubic interpolation as in [44, 53, 74], outlining the relevant modifications needed for the sphere. Thereafter, we explain how the spatial interpolation and time integration are incorporated to evolve the backward characteristic map within the GALS framework along with additional details on the computational implementation.

3.3.1 Gradient-Augmented Level Set Method

The GALS method falls under the class of semi-Lagrangian methods for the numerical solution of the advection equation. It employs an advect-and-project strategy, where the temporal evolution of the numerical quantity of interest is evolved in the Lagrangian frame and then projected back, using a suitable interpolation operator, onto a static Eulerian grid [44]. The method is part of a more general class of numerical methods, referred to as *jet schemes* [53], where derivative information, along with the function values, are additionally transported to obtain higher-order accuracy. Unlike ENO/WENO

schemes [34, 55], which use wide stencils along each coordinate direction to achieve higher-order accuracy, jet schemes use localized stencils whose evaluation is facilitated by interpolation. A key ingredient of the GALS method is an optimally local update procedure achieved in the projection step by using information from a single adjacent cell for function values and derivatives. We begin by describing the spatial discretization of the backward characteristic map using Hermite cubics. Thereafter, we explain how gradient information is transported during the time integration to achieve a scheme that is globally third-order accurate.

3.3.2 Spatial Discretization

The spatial discretization of the backward characteristic map is performed using Hermite cubic interpolation. Techniques for interpolation on the 2-sphere have been the subject of extensive study (cf. [19]). We employ a cell-based interpolation directly on the (λ, θ) parametric space on a rectangular grid, similar to the construction of [71]. The use of a rectangular grid allows for a tensor product spline approach [17,52]. Here we consider, a tensor product of Hermite cubics. Let Ω denote our computational domain, taken as an uniform partition of the doubled-up coordinate chart $(\lambda, \theta) \in [-\pi, \pi] \times [-\pi, \pi]$. Let the gridpoints $\varphi_{i,j} = (\lambda_i, \theta_j)$ be defined by

$$\lambda_i = -\pi + i\frac{2\pi}{N} \ , \ \theta_j = -\pi + j\frac{2\pi}{N} \quad \text{for } i, j \in \{0, \dots, N-1\}. \tag{3.12}$$

Let $C_{i,j}$ be a cell within the partition with corners $\varphi_{i,j}$, $\varphi_{i+1,j}$, $\varphi_{i,j+1}$ and $\varphi_{i+1,j+1}$. The space of Hermite cubics on Ω, denoted $\mathcal{V}_\Omega$, is a subspace of $C^1(\Omega)$ functions which are bicubic in each cell with continuous normal derivatives and smooth tangential derivative on cell boundaries. The local interpolation operator $H_\Omega[f] : C^1(\Omega) \to \mathcal{V}_\Omega$, is defined such that

$$D^\alpha f(\varphi_{i,j}) = D^\alpha H_\Omega[f](\varphi_{i,j}) \quad \forall \varphi_{i,j} \in \Omega \ , \tag{3.13}$$

for multi-index α part of the index set $\alpha \in \{(1,0), (0,1), (1,1)\}$. In one dimension, if we consider the vertex set $i \in \{0, 1\}$, then the basis functions satisfying the properties of an Hermite interpolant are given by

$$H_i^\alpha(x) = \begin{cases} f(x) & \text{for } i = 0, \ \alpha = 0 \, , \\ f(1-x) & \text{for } i = 1, \ \alpha = 0 \, , \\ g(x) & \text{for } i = 0, \ \alpha = 1 \, , \\ -g(1-x) & \text{for } i = 0, \ \alpha = 1 \, , \end{cases} \tag{3.14}$$

where $f(x) = 1-3x^2+2x^2$ and $g(x) = x(1-x)^2$. The 2D basis functions are then defined in each cell $C_{i,j}$ in the extended computational domain $(\lambda, \theta) \in [-\pi, \pi]^2$ via translation and scaling as

$$H^{\alpha}_{i,j}(\lambda,\theta) = H^{\alpha_1}_i\left(\frac{\lambda-\lambda_{i,j}}{\Delta\lambda_i}\right) H^{\alpha_2}_j\left(\frac{\theta-\theta_{i,j}}{\Delta\theta_j}\right)\Delta\phi^{\alpha_1}\Delta\theta^{\alpha_2} \tag{3.15}$$

The local interpolating polynomial for a point φ lying within the cell $C_{i,j}$, is then given by

$$H_\Omega[f](\varphi) = \sum_{i,j}\sum_{\alpha} f^{\alpha}_{i,j} H^{\alpha}_{i,j}\left(\frac{\varphi}{\Delta\varphi}\right)\Delta\varphi^{\alpha}\,, \tag{3.16}$$

where $f^{\alpha}_{i,j}$ are the values of the function, its partial and mixed partial derivatives in the cell $C_{i,j}$. We now investigate some of the approximation properties of the interpolant.

Lemma 3.1. Denote δu the error in quantity u and let the data $f^{\alpha}_{i,j}$ in 3.16 be known to $\mathcal{O}(h^{4-|\alpha|})$ for multi-index $\alpha \in \{(1,0),(0,1),(1,1)\}$ and h being the maximum grid spacing. Then the error in $H_\Omega[f](\lambda,\theta)$ is given by

$$\delta H_\Omega[f](\varphi) = \sum_{i,j}\sum_{\alpha} \delta f^{\alpha}_{i,j} H^{\alpha}_{i,j}\left(\frac{\varphi}{\Delta\varphi}\right)\Delta\varphi^{\alpha} \tag{3.17}$$

and have that the error $\delta\left(D^{\alpha}H_\Omega[f](\varphi)\right) = \mathcal{O}(h^{4-|\alpha|})$.

Proof. Every f^{α} is multiplied by $\Delta\varphi^{\alpha}$ increasing the order accuracy by $h^{|\alpha|}$, similarly for every derivative $D^{\alpha}H$ the order of accuracy decreases due to the scaling by $\Delta\varphi$ by at least $\mathcal{O}(h^{-|\alpha|})$. □

Theorem 3.2. Let $f \in C^4(\Omega)$, and the data $f^{\alpha}_{i,j}$ in 3.16 be known to order $h^{4-|\alpha|}$, where h is the spacing of the largest cell. Then the $L^\infty(\Omega)$ error can be bounded as

$$\|f - H_\Omega[f]\|_{L^\infty(\Omega)} \leq c\left\|D^4 f\right\|_{L^\infty(\Omega)} h^4\,. \tag{3.18}$$

Proof. Let $G(\boldsymbol{x})$ be the Taylor polynomial of order three for f centred at the point $\varphi_0 \in C_{i,j}$. By Taylor's theorem, for all $\phi \in C_{i,j}$, we have

$$D^{\alpha}f(\varphi) = D^{\alpha}G(\varphi) + \mathcal{O}(h^{4-|\alpha|})\,, \tag{3.19}$$

yielding,

$$\begin{aligned}\|f - H_\Omega[f]\|_{L^\infty(\Omega)} &\leq \|f-G\|_{L^\infty(\Omega)} + \|G - H_\Omega[f]\|_{L^\infty(\Omega)} \\ &= \mathcal{O}(h^4) + \|G - H_\Omega[f]\|_{L^\infty(\Omega)}\,.\end{aligned} \tag{3.20}$$

By construction, since G approximates the data $f^{\alpha}_{i,j}$ at the vertices to $\mathcal{O}(h^{4-\alpha})$ we have that $G(\varphi)$ and $H_\Omega[f](\varphi)$ are related by Lemma 3.1 and thus $|G - H_\Omega[f]| = \mathcal{O}(h^4)$ $\forall\varphi \in C_{i,j}$. □

Since this holds in any particular cell, the approximation error also holds over the whole space. The order of accuracy in $L^2(\mathbb{S}^2)$ is then readily obtained by noting,

$$\|f - H_\Omega[f]\|^2_{L^2(\mathbb{S}^2)} = \int_0^\pi \int_{-\pi}^\pi |f - H_\Omega[f]|^2 \sin(\theta) d\lambda \, d\theta \leq 4\pi \, \|f - H_\Omega[f]\|^2_{L^\infty(\Omega)} \,, \tag{3.21}$$

$$\Rightarrow \|f - H_\Omega[f]\|_{L^2(\mathbb{S}^2)} \leq Ch^4 \tag{3.22}$$

We note that the condition on $f \in C^4(\Omega)$ can be relaxed in regularity but will not be needed for our purposes. Since we only require an accuracy of $\mathcal{O}(h^{4-|\alpha|})$ for the values of $D^\alpha f(\lambda_i, \theta_j)$ it suffices to use approximate values. The GALS method exploits this property to transport derivative information at the grid points up to order of accuracy required. The approximation is of the derivative information is performed using a 4-point ϵ-difference stencil about each grid point. The approximated values of $f^\alpha_{i,j}$ are given by

(3.23)

$$\begin{aligned}
f^{0,0}_{i,j} &= \frac{1}{4}\left(f(\lambda_i + \epsilon, \theta_j - \epsilon) + f(\lambda_i - \epsilon, \theta_j - \epsilon) + f(\lambda_i + \epsilon, \theta_j + \epsilon) + f(\lambda_i - \epsilon, \theta_j + \epsilon)\right) \\
f^{1,0}_{i,j} &= \frac{1}{4\epsilon}\left(f(\lambda_i + \epsilon, \theta_j - \epsilon) - f(\lambda_i - \epsilon, \theta_j - \epsilon) + f(\lambda_i + \epsilon, \theta_j + \epsilon) - f(\lambda_i - \epsilon, \theta_j + \epsilon)\right) \\
f^{0,1}_{i,j} &= \frac{1}{4\epsilon}\left(f(\lambda_i + \epsilon, \theta_j + \epsilon) - f(\lambda_i + \epsilon, \theta_j - \epsilon) + f(\lambda_i - \epsilon, \theta_j + \epsilon) - f(\lambda_i - \epsilon, \theta_j - \epsilon)\right) \\
f^{1,1}_{i,j} &= \frac{1}{4\epsilon^2}\left(f(\lambda_i + \epsilon, \theta_j + \epsilon) - f(\lambda_i + \epsilon, \theta_j - \epsilon) - f(\lambda_i - \epsilon, \theta_j + \epsilon) + f(\lambda_i - \epsilon, \theta_j - \epsilon)\right)
\end{aligned}$$

To quantify the order of approximation obtained in 3.23 by using a Taylor series expansion to second-order, we must first determine expressions for the gradient and Hessian matrix in the spherical coordinate system. If we consider $\mathbb{S} \subset \mathbb{R}^3$ and take the restriction of the Euclidean metric in $\mathbb{R}^3$, $ds^2 = dx^2 + dy^2 + dz^2$, to the unit sphere, we obtain the metric

$$ds^2 = \sin^2(\theta) d\lambda^2 + d\theta^2 \tag{3.24}$$

For any point $p \in \mathbb{S}^2$ away from the poles, if we denote the the unit tangent vectors in the direction of increasing longitude and latitude as e_λ, e_θ respectively, then we have

$$\partial_\lambda = \sin(\theta) e_\lambda, \quad \partial_\theta = e_\theta \,. \tag{3.25}$$

Thus $\{\partial_\lambda / \sin(\theta), \partial_\theta\}$ form an orthonormal basis for the tangent plane $T_p\mathbb{S}^2$. The gradient of the local representative of a function $f : \mathbb{S}^2 \to \mathbb{R}$ in the spherical coordinate system is given by

$$\nabla_{\mathbb{S}^2} f(\lambda, \theta) = \left[\frac{1}{\sin(\theta)} \partial_\lambda f, \partial_\theta f\right]^T . \tag{3.26}$$

Generally, the Hessian matrix of a C^2 function f on a Riemannian manifold, with local coordinates x is

$$\text{Hess}(f) = \left(\frac{\partial^2 f}{\partial x^i \partial x^j} - \Gamma^k_{i,j} \frac{\partial f}{\partial x^k} \right) dx^i \otimes dx^j \,, \tag{3.27}$$

where the Christoffel symbols are given by

$$\Gamma^k_{i,j} = \frac{\partial e_i}{\partial x^j} g^{kl} e_l. \tag{3.28}$$

Using the Riemannian metric on the sphere and the expressions 3.25, we have

$$\text{Hess}(f) = \begin{bmatrix} \partial_{\lambda\lambda} f + \cos(\theta)\sin(\theta)\partial_\theta f & \partial_{\lambda\theta} f - \frac{\cos(\theta)}{\sin(\theta)} \partial_\lambda f \\ \partial_{\lambda\theta} f - \frac{\cos(\theta)}{\sin(\theta)} \partial_\lambda f & \partial_{\theta\theta} f \end{bmatrix}. \tag{3.29}$$

Thus the Taylor expansion of a smooth function f on the sphere about a point $\bar{\varphi}$ away from the poles is

$$\begin{aligned} f(\varphi) &= f(\bar{\varphi}) + \nabla f|_{\bar{\varphi}} \cdot (\varphi - \bar{\varphi}) + \frac{1}{2} (\varphi - \bar{\varphi})^T \, Hess(f)|_{\bar{\varphi}} \, (\varphi - \bar{\varphi}) + \mathcal{O}((\varphi - \bar{\varphi})^3) \\ &= f(\bar{\varphi}) + \frac{1}{\sin(\bar{\theta})} \, \partial_\lambda f|_{\bar{\varphi}} \, (\lambda - \bar{\lambda}) + \partial_\theta f|_{\bar{\varphi}} \, (\theta - \bar{\theta}) \\ &+ \left(\partial_{\lambda\theta} f|_{\bar{\varphi}} - \frac{\cos(\bar{\theta})}{\sin(\bar{\theta})} \, \partial_\lambda f|_{\bar{\varphi}} \right) (\theta - \bar{\theta})(\lambda - \bar{\lambda}) + \mathcal{O}((\varphi - \bar{\varphi})^2). \end{aligned} \tag{3.30}$$

Due to finite-precision arithmetic used in the evaluations of the expressions in 3.23, an error due to round-off will be incurred for each of the stencils points. Using double-precision floating point numbers, the numerical precision, denoted δ, for which a number can be computed is $2^{-52} \approx 2.22 \times 10^{-16}$. To observe the effect of round-off error on the precision of the derivatives, we consider a Taylor expansion of $f(\lambda, \theta)$ about a point (λ_i, θ_j) away from the poles, evaluating at the epsilon difference stencil points. For the value of $f^{1,0}_{i,j}$, this yields

$$\begin{aligned} f^{1,0}_{i,j} &= \nabla f|_{\varphi_{i,j}} \cdot ((\epsilon + \delta)/\epsilon, \delta/\epsilon)^T + \mathcal{O}(\epsilon^2) \\ &= \frac{1}{\sin(\theta_j)} \partial_\lambda f(\varphi_{i,j}) + \left(\frac{1}{\sin(\theta_j)} \partial_\lambda f(\varphi_{i,j}) + \partial_\theta f(\varphi_{i,j}) \right) \frac{\delta}{\epsilon} + \mathcal{O}(\epsilon^2) \,, \end{aligned} \tag{3.31}$$

and this holds analogously for $f^{0,1}_{i,j}$. For the mixed partial derivatives, which we denote $\text{Hess}(f)_{1,1}$, noting that for each evaluation δ is not necessarily the same, we have

$$\begin{aligned} f^{1,1}_{i,j} &\approx \frac{1}{4\epsilon^2} \text{Hess}(f)_{1,1}(\varphi_{i,j}) \left[(\epsilon + \delta)(\epsilon + \delta) - 2(\epsilon + \delta)(-\epsilon + \delta) + (\epsilon + \delta)(-\epsilon + \delta) \right] \\ &+ \frac{1}{4\epsilon^2} \left(\frac{1}{\sin(\theta_j)} \, \partial_\lambda f|_{\varphi_{i,j}} \, 4\delta + \partial_\theta f(\varphi_{i,j}) 4\delta \right) + \mathcal{O}(\epsilon^2) \\ &= \text{Hess}(f)_{1,1}(\varphi_{i,j}) \left(1 + \frac{\delta}{\epsilon} + \frac{\delta^2}{\epsilon^2} \right) + \left(\frac{1}{\sin(\theta_j)} \partial_\lambda f(\varphi_{i,j}) + \partial_\theta f(\varphi_{i,j}) \right) \frac{\delta}{\epsilon^2} + \mathcal{O}(\epsilon^2) \end{aligned} \tag{3.32}$$

We see that the truncation error decreases asymptotically to ϵ^2 yet the error due to round-off increases proportionally to $1/\epsilon$ for the gradient and $1/\epsilon^2$ for the mixed partial derivatives. This bears constraints on preserving the correct order of accuracy in the derivative information for the Hermite interpolant. Namely, in order to remain consistent with the $\mathcal{O}(h^4)$ in the local truncation error in the Hermite interpolation one must choose ϵ appropriately. To retain an $\mathcal{O}(h^3)$ accuracy in the gradient values, one could scale $\epsilon \propto h^{3/2}$ whereas for the mixed partial derivatives require $\epsilon \propto h$. Yet, if the scaling is implemented, the round-off error will increase. In practice, we take $\epsilon = 10^{-5}$, setting an 'effective numerical precision' to be approximately $\delta_\epsilon \approx 10^{-11}$.

If we additionally require that the velocity field have vanishing azimuthal derivative at the poles, then the approximation properties still hold. A global parameterization using only the basis vectors e_λ, e_θ for more general vector fields on the surface of the sphere, will not suffice due to their degeneracy at the poles. For linear advection, the coordinate singularity manifests itself as a difficulty when calculating Lagrangian particles trajectories near the poles. The coordinate singularity inherent in the spherical coordinate system has been the subject of extensive study notably in the atmospheric modelling community [56,59–61]. Presently, the problem is often circumvented by instead performing the trajectory computations in the Cartesian system as done in [11, 54]. The velocity fields that we consider in the forthcoming numerical tests vanish at the poles and the resulting flows can thus be well-represented as a $C^1(\Omega)$ function in the standard spherical coordinate system. In the forthcoming chapter, we offer some possible alternatives to circumvent the issues related to the spherical coordinate system.

3.3.3 Time Evolution

In the spherical coordinate system, the advection equation is given by

$$\partial_t \phi + \frac{u_\lambda}{\sin(\theta)} \partial_\lambda \phi + \partial_\theta \phi = 0\,. \tag{3.33}$$

The characteristic (integral) curves, $\boldsymbol{\gamma}(t) = (\lambda(t), \theta(t))^T$, are given by

$$\begin{aligned} \frac{\mathrm{d}\lambda}{\mathrm{dt}} &= \frac{u_\lambda(\boldsymbol{\gamma}(t), t)}{\sin(\theta)}\,, \\ \frac{\mathrm{d}\theta}{\mathrm{dt}} &= u_\theta(\boldsymbol{\gamma}(t), t)\,, \\ \boldsymbol{\gamma}(0) &= \boldsymbol{\gamma}_0\,. \end{aligned} \tag{3.34}$$

The solution is obtained using 3.4 by approximating the backward characteristic map using a finite amount of integral curves $\gamma_{i,j}$. Each iteration $t_n \mapsto t_{n+1}$ introduces a set

of Lagrangian particles at the grid points, that is, $\gamma_{i,j}(t_n) = \varphi_{i,j}$, whose trajectories are computed backwards in time using a globally third-order Runge-Kutta integration scheme. Introducing the particles at the grid points at each time step allows us to maintain a representation of the map on the fixed Eulerian grid. The values obtained from these trajectories serve to update the global inverse flow map via composition with the previous map at the endpoint of the trajectories; a discrete analogue of 3.8. In order for this process to be iterated, we must project back onto the space of Hermite cubics after evaluation, obtaining a map which can once again be evaluated at an arbitrary point.

Let $\chi_i(\boldsymbol{x}, t)$ denote the projection of $X_i^{-1}(\boldsymbol{x}, t)$ onto the space of Hermite cubics. Then each time step of the CM method is summarized as follows:

$$\begin{aligned} \Psi &= \varphi + \int_{t_{n+1}}^{t_n} \boldsymbol{G}\tilde{u}(\gamma(s), s)\mathrm{d}s\,, \\ \chi_i(\varphi, t) &= H_\Omega[\chi_i \circ (\Psi, t_n)]\,, \end{aligned} \tag{3.35}$$

$$\chi_{[t_{n+1},0]}(\boldsymbol{x}, t) = \chi_{[t_n,0]} \circ \chi_{[t_{n+1},t_n]}(\boldsymbol{x}, t). \tag{3.36}$$

where $\boldsymbol{G}$ is the matrix given by

$$\boldsymbol{G} = \begin{bmatrix} \frac{1}{|\sin(\theta)|} & 0 \\ 0 & 1 \end{bmatrix}. \tag{3.37}$$

We note that the absolute value accounts for the use of the negative values for θ in the doubled up coordinate chart preserving the positivity of the metric.

In order to implement the projection step, gradient and mixed partial derivative information must be transported along with the function values. This is accomplished by additionally introducing Lagrangian particles in a 4-point ϵ-difference stencil at the grid points and integrating for their footpoints. The map is evaluated at the location of the footpoints and the derivative information is updated using the stencils 3.23. Additionally, the footpoint of the grid point itself is solved for, determining the cell in which the footpoints from the stencil are evaluated. If the stencil point lands outside the cell in which the grid point lands, then the basis functions are simply extended outside to accommodate. Since the integration scheme is of matching order in local truncation error to the Hermite interpolation, the transported ϵ-difference stencil retains the order of accuracy required by 3.1, and maintains a $\mathcal{O}(h^4)$ accurate interpolant. The implementation of the algorithm is summarized in algorithm 1 1.

Algorithm 1: Characteristic Mapping Method

Input: u, $[0, \mathrm{t}_1, \ldots, T], \epsilon, \Omega = [\varphi_{i,j}]$

Output : χ

Initialization: $\chi_0 \leftarrow H_\Omega[\chi]([\varphi_{i,j}]) = \mathrm{id}$, $t = 0$

while $t < T$ **do**

$y = [\varphi_{i,j} \pm \epsilon]$ % initialize stencil points and grid point

$[\Psi_{i,j} \pm \epsilon]_t \leftarrow RK3(\mathrm{u}, \mathrm{t}, \Delta t, y)$

$[D^\alpha \chi_{i,j}]_t \leftarrow \chi([\Psi_{i,j} \pm \epsilon]_t)$ according to 3.23

$\chi_{[t,0]} \leftarrow H_\Omega[[D^\alpha \chi_{i,j}]_t]$

$\mathrm{t} \leftarrow t + \Delta t$

end

return $_{[t,0]}$

The numerical computation of 3.35 incurs two errors in each step; an $\mathcal{O}(\Delta t^4)$ error due to the local truncation error in the time-integration and an $\mathcal{O}(\Delta t^2 \Delta x^2)$ due to the projection step. As previously noted, for the ϵ-difference stencilling, if we neglect the error due to round-off then the error scales quadratically in the distance between the point of evaluation and the nearest grid point. For each of the grid points, the evaluation $\chi_i \circ (\Psi, t_n)$ for the projection step occurs at foot points $\mathcal{O}(\Delta t)$ away and a distance $\mathcal{O}(\Delta x)$ away from the nearest grid point, resulting in the $\mathcal{O}(\Delta t^2 \Delta x^2)$ accuracy [36]. Globally, the method is third-order accurate, with error given by

$$\text{Global error for GALS} = \mathcal{O}(T\Delta t^3) + \mathcal{O}(T\Delta t \Delta x^2)\,. \tag{3.38}$$

In the forthcoming sections we present convergence tests for our implementation of the CM method for linear advection on the sphere. We affirm the aforementioned approximation properties of the method using a standard test cases for the transport equation on the sphere. Thereafter, we demonstrate its ability to resolve arbitrarily fine features in the solution along with the capacity to advect arbitrary sets.

3.4 Numerical Tests

In this section we present convergence tests for the numerical solution of 3.1 and 3.6 using the CM method. These test cases follow a standard test case suite for linear transport on the sphere as outlined in [41, 42] involving linear and non-linear flows.

3.4.1 Initial Conditions

In what follows, for consistency with the literature, we define $(\lambda, \theta) \in [0, 2\pi] \times [-\pi/2, \pi/2]$ and the corresponding components of the advecting velocity field are denoted by u and v. All of the flows, with the exception of test case 2, are designed such that the initial condition returns to itself after a predetermined amount of time. In the following tests we consider two different initial conditions. The first of which is two symmetrically located cosine-bells, defined by

$$h_i(\lambda, \theta) = \begin{cases} \frac{1}{2}\left[1 + \cos(\pi r_i / r)\right] & \text{if } r_i < r\,, \\ 0 & \text{otherwise}\,, \end{cases} \tag{3.39}$$

where $r = 1/2$ is taken to be the base radius of each cosine bell and $r_i = r_i(\lambda, \theta)$ is the great-circle distance from the centre of the bell, given by

$$r_i(\lambda, \theta) = \arccos(\sin\theta_i \sin\theta + \cos\theta_i \cos\theta \cos(\lambda - \lambda_i))\,, \tag{3.40}$$

with (λ_i, θ_i) being the location of the centre of the bell. The initial condition is then given by

$$\phi(\lambda, \theta) = b + h_1(\lambda, \theta) + h_2(\lambda, \theta)\,, \tag{3.41}$$

where $b = 0.1$ and the centres of each bell are located at $(\lambda_1, \theta_1) = (\pi/6, 0)$ and $(\lambda_2, \theta_2) = (-\pi/6, 0)$. The second condition we consider is two slotted cylinders, defined by

$$\phi(\lambda, \theta) = \begin{cases} 1 & \text{if } r_i \le r \text{ and } |\lambda - \lambda_i| \ge r/6 \text{ for } i = 1, 2\,, \\ 1 & \text{if } r_i \le r \text{ and } |\lambda - \lambda_1| < r/6 \text{ and } \theta - \theta_1 < -\frac{5}{12} r\,, \\ 1 & \text{if } r_i \le r \text{ and } |\lambda - \lambda_2| < r/6 \text{ and } \theta - \theta_2 > \frac{5}{12} r\,, \\ 0.1 & \text{otherwise}\,. \end{cases} \tag{3.42}$$

This initial quantity is designed to assess the shape-preserving properties of the method. We assess the accuracy of the method by computing the error in the following norms

$$\begin{aligned} \|f(\lambda_i, \theta_j, t)\|_{\ell^\infty(\Omega)} &= \max_{i,j}\{|f(\lambda_i, \theta_j, t)|\}\,, \\ \|f(\lambda_i, \theta_j, t)\|_{\ell^2(\Omega)} &= \left(\sum_i^N \sum_j^N f(\lambda_i, \theta_j, t)^2 \Delta\lambda \Delta\theta \sin(\theta_j)\right)^{1/2}, \end{aligned} \tag{3.43}$$

where $\Delta\lambda$ and $\Delta\theta$ are the grid spacings in the azimuthal and polar directions respectively and (λ_i, θ_j) for $i, j = 1, \ldots, N$ are grid points within the computational domain.

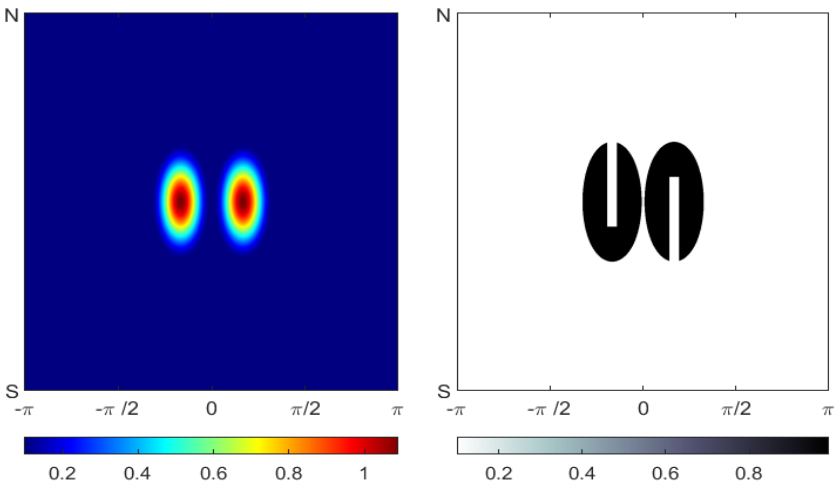

Figure 3.1: Cosine bell and slotted cylinder initial conditions

3.4.2 Test Case 1: Solid Body Rotation

The first test case we consider is the solid body rotation as described in [70] for a rotation axis aligned with the north pole. The advecting velocity field and stream function are given by

$$\begin{aligned} u_1 &= u_0 \cos\theta\,, \\ v_1 &= 0\,, \\ \psi_1 &= -u_0 \sin\theta\,, \end{aligned} \tag{3.44}$$

where the coefficient u_0 is chosen to be 2π such that one full rotation corresponds to a final integration time of $t = 1$ units. We note that variants of this test consider rotation about axes that are not aligned with the pole. If the poles of the coordinate system are not aligned with the axis of rotation, then the advecting velocity field will be multi-valued there. To remedy the inevitable error this will cause by working in the coordinate system, one can change the coordinate system to one in which the poles are aligned with the axis of rotation [41]. The backward characteristic map is given analytically by

$$\chi(\lambda, \theta, t) = (\lambda - 2\pi t, \theta)\,. \tag{3.45}$$

In this instance, since the exact backward characteristic map is a linear function, the approximation via an Hermite cubic is exact to within numerical precision. Consequently, the dominant contribution to the error is due to round-off which is dictated by the ϵ-difference stencil. Typically, the contribution due to the stencilling is much less than the error incurred by the discretization of the flow but in this test using a linear and one dimensional flow, the two errors are approximately the same magnitude. Since at every

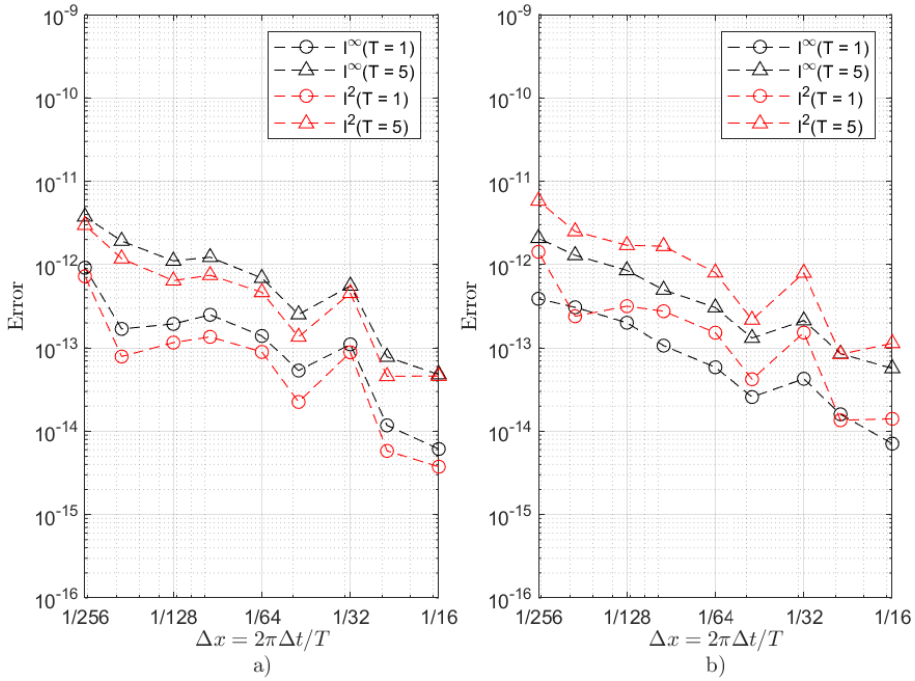

Figure 3.2: Error in solution (a) for the cosine-bell and χ_λ map (b) for test case 1 for a final time $T = 1$ and $T = 5$. The error in the numerical solution for the slotted cylinder is not included since it is identically zero.

step we redefine an Hermite interpolant for the flow-map using the stencil, we expect the error to increase with the number of time steps. Figure 3.10 depicts the accumulation of the round-off error in the ϵ-difference stencils as the number of time-steps increases.

3.4.3 Test Case 2: Static Vortex

For the second test case we consider a deformational flow consisting of two steady circular vortices with antipodal centres, as described in [41]. Since the vortices are generated symmetrically on the sphere, we need only consider one vortex. Denoting $\rho = \rho_0 \cos(\theta)$, the radial distance from the centre of the vortex, the angular velocity in dimensionless units is given by

$$\omega(\theta) = \begin{cases} \frac{2\pi}{T}\frac{3\sqrt{3}}{2\rho}\mathrm{sech}^2(\rho)\tanh(\rho) & \text{if } \rho \neq 0\,, \\ 0 & \text{if } \rho = 0. \end{cases} \tag{3.46}$$

The analytic backward characteristic map is now given by $\boldsymbol{\chi}(\lambda, \theta, t) = (\lambda - w_r(\theta)t, \theta)$. The velocity components are then written as

$$\begin{aligned} u(\lambda,\theta) &= \omega(\theta)\left[\sin(\theta_c)\cos(\theta) - \cos(\theta_c)\cos(\lambda-\lambda_c)\sin(\theta)\right]\,, \\ v(\lambda,\theta) &= \omega(\theta)\left[\cos(\theta_c)\sin(\lambda-\lambda_c)\right]\,, \end{aligned} \tag{3.47}$$

where (λ_c, θ_c) is the position of the centre of the vortex. The solution for all time is given by

$$\phi(\lambda, \theta, t) = 1 - \tanh\left[\frac{\rho}{5}\sin(\lambda - \omega(\theta)t)\right], \tag{3.48}$$

where the coefficients $1/5$ along with $\rho_0 = 3$ are chosen so that the deformation in the flow is smooth [40, 43].

The static vortex test consists of a flow which now depends non-linearly on the latitudinal coordinate. Thus the flow map will not be represented exactly using a bivariate third order polynomial. We note that the computations are only performed on the displacement map, that is, we need only consider the displacement of the map from the identity map. Since the flow in the latitudinal direction is the identity map for this test case, the displacement is identically zero for all time. The map is thus represented exactly and we encounter no round-off error in the latitudinal direction.

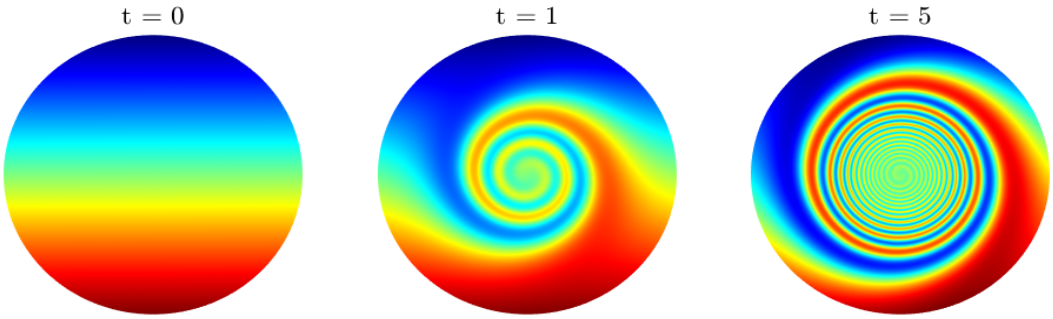

Figure 3.3: Depiction of the numerical solution for test case 2 at times $t = 0, 1, 5$. View is taken top down with the centre being the north pole.

Since the computational domain represents the north pole as an entire line, we do not include the north pole as a point on our grid. This prevents the advection of what should be a point as a line across the domain during the numerical solution. Nevertheless, the characteristic map is indeed defined at the poles, and allowed to be multi-valued. Since the initial condition itself is not multi-valued at the poles, the pullback of the initial condition via the backward characteristic map will not be multi-valued.

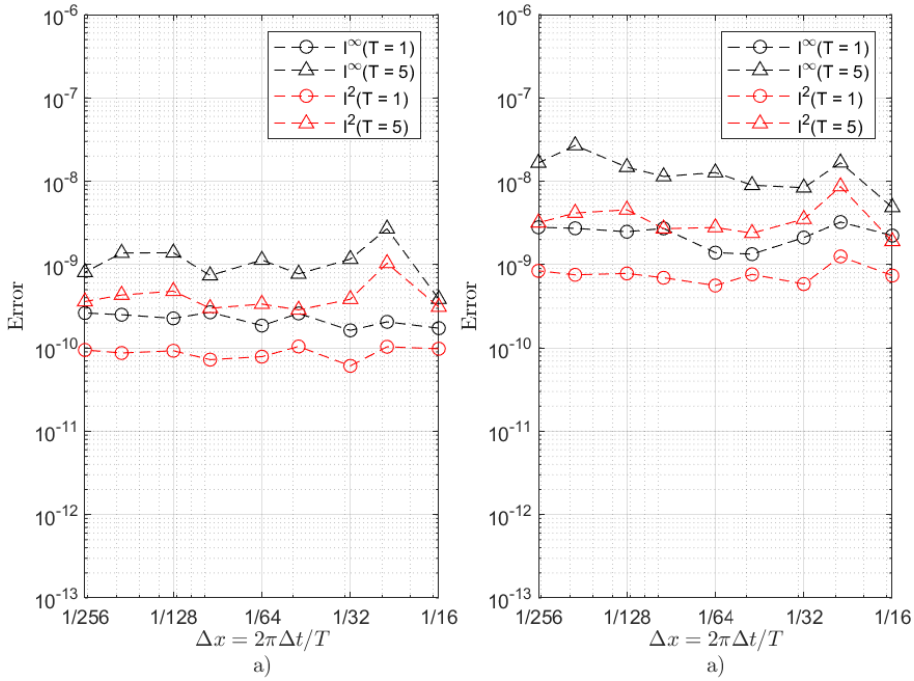

Figure 3.4: Error in solution and the χ_λ map for test case 2 for a final time $T = 1, 5$

3.4.4 Test Case 3: Non-Divergent Flow

The next test cases present flows which are now non-linear in both directions. The first of which is a divergence free flow as given in [42], in the form

$$\begin{aligned} u_2(\lambda,\theta,t) &= k\sin^2(\lambda)\sin(2\theta)\cos(\pi t/T)\,, \\ v_2(\lambda,\theta,t) &= k\sin(2\lambda)\cos(\theta)\cos(\pi t/T)\,, \\ \psi_2(\lambda,\theta,t) &= k\sin^2(\lambda)\cos^2(\theta)\cos(\pi t/T)\,. \end{aligned} \tag{3.49}$$

The advecting field is designed such that the initial condition returns to its original position at time $t = T$. Since the advected scalar field travels along the same flow lines in reverse after $t = T/2$, there is a possibility for cancellation of error. This can be avoided by considering a background flow that rotates the deforming field such that one full rotation coincides with the time it takes for a trajectory to return back to its starting point [42]. The effective velocity field and stream function are given by

$$\begin{aligned} u_3(\lambda,\theta,t) &= k\sin^2(\lambda-2\pi t/T)\sin(2\theta)\cos(\pi t/T) + 2\pi\cos(\theta)/T \\ v_3(\lambda,\theta,t) &= k\sin(2(\lambda-2\pi t/T))\cos(\theta)\cos(\pi t/T) \\ \psi_3(\lambda,\theta,t) &= k\sin^2(\lambda-2\pi t/T)\cos^2(\theta)\cos(\pi t/T) - 2\pi\sin(\theta)/T \end{aligned} \tag{3.50}$$

The results of this test with and without a background flow are depicted in Figure 3.5. Due to the non-linearity of the flow in both directions, the numerical solution is not

significantly affected by the round-off error in the epsilon derivative. We thus observe the theoretically expected convergence rate for both flows.

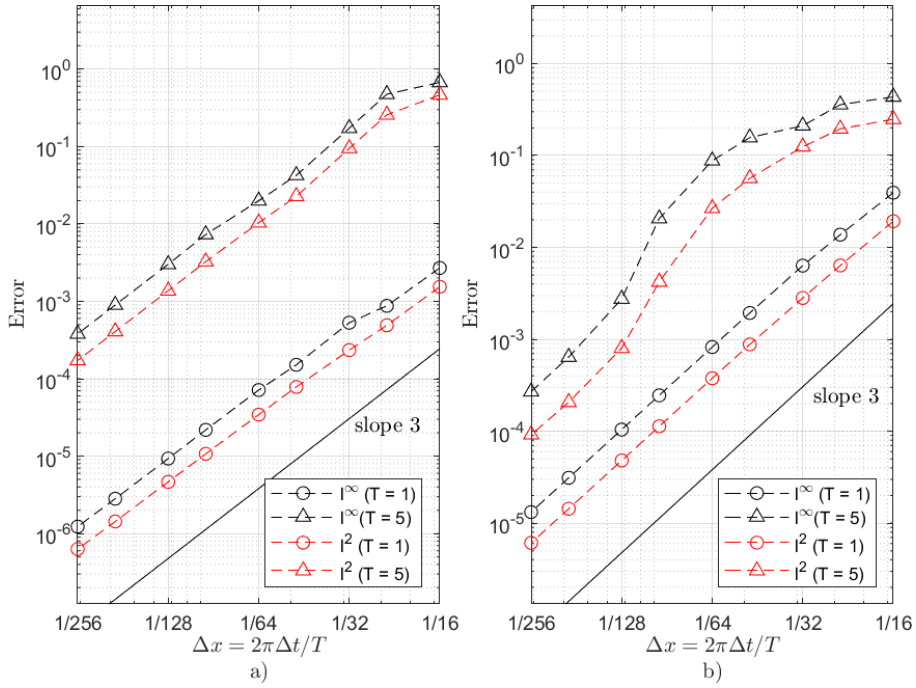

Figure 3.5: Error in solution without (a) and with (b) background flow at $T = 1, 5$.

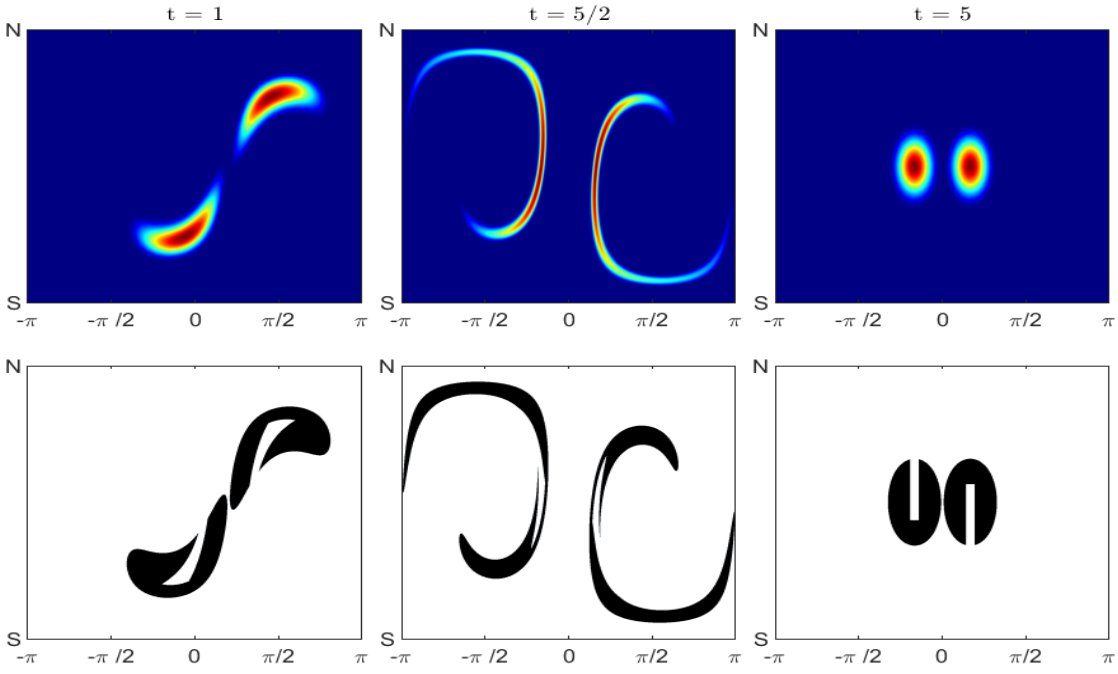

Figure 3.6: Depiction of the numerical solution for the cosine-bell and slotted cylinder with an advecting field 3.50 at times $t = 1, 2.5, 5$.

3.4.5 Test Case 4: Divergent flow

As a final numerical test we consider a divergent flow, in the form

$$
\begin{aligned}
u(\lambda,\theta,t) &= -\sin^2(\lambda/2)\sin(2\theta)\cos^2(\theta)\cos(\pi t/T) \\
v(\lambda,\theta,t) &= \frac{1}{2}\sin(\lambda)\cos^3(\theta)\cos(\pi t/T)
\end{aligned} \tag{3.51}
$$

Since the flow is no longer divergence free, the compressibility of the map is incorporated by multiplication of the initial condition by the determinant of the Jacobian of the map at time t. This quantity measures the deformation of the volume element due to the compressibility of the flow and can be computed directly from the Hermite basis functions. The effect of the divergence in the flow, is observed in Figure 3.7, where the domain can be seen to be stretching. For the slotted cylinder this is most apparent, where the solution takes values in between its piecewise constant initial values.

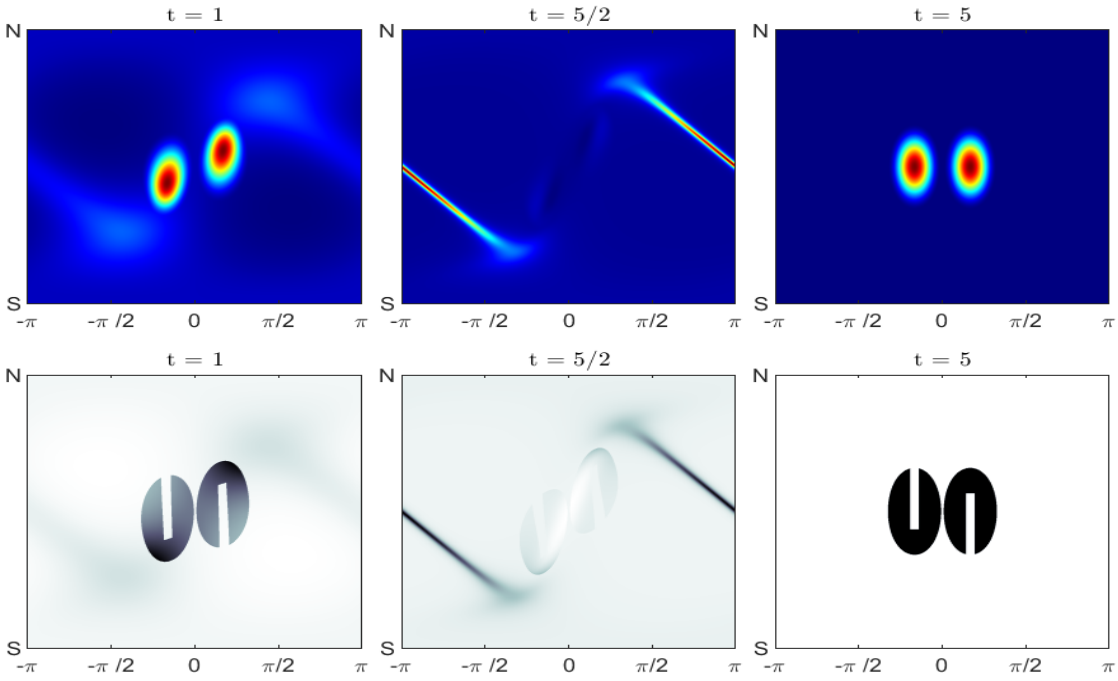

Figure 3.7: Depiction of the numerical solution for test case 4 at times $t = 1, 2.5, 5$.

3.5 Arbitrary Set Advection and Subgrid Resolution

In this section we demonstrate two unique features of the CM method: the ability to advect arbitrary sets and subgrid resolution. Since the solution is given by the pullback of the initial condition by the backward characteristic map, the method has the ability to represent the transport of an initial condition up to the precision for which the initial condition is known. In the idealized cases considered, the initial conditions are given

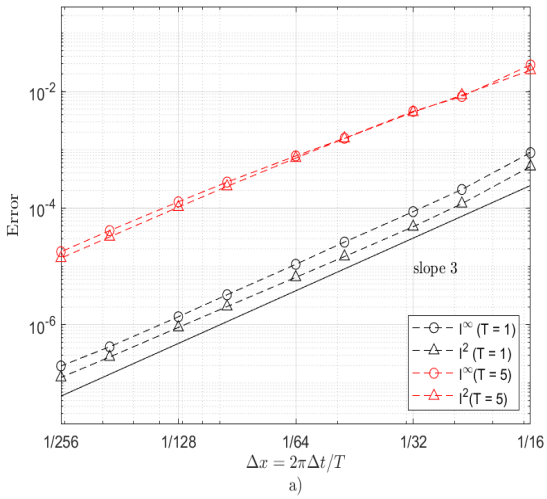

Figure 3.8: Error in solution for test case 4 for a final time $T = 1$ and $T = 5$ in the ℓ^∞ and ℓ^2 norms without any remapping steps.

analytically and therefore arbitrarily fine features can be represented in the solution. Moreover, since the deformational map is defined everywhere in space, we can 'zoom-in' on the solution at any point in time by evaluating the map on the region, thus achieving exponential resolution in linear computation time. We depict this unique feature of the method with a zoom-in on the numerical solution for an initial condition possessing multiple scales smaller than the numerical grid for which the computation is performed on. Thereafter we demonstrate the advection of the Mandelbrot set as defined on the sphere. This serves to emphasize the capacity to transport arbitrarily defined quantities along with offering a depiction of a drift in the map at scales proportional to the L^∞ error for the advection of a smooth function or the map itself.

In order to illustrate the capacity of the method to represent fine-features in the advected quantity, we consider an initial condition of the form

$$\phi(\lambda,\theta) = \cos(10\lambda)\sin(10\theta) - \cos(100\lambda)\sin(100\theta) + 0.1\cos(1000\lambda)\sin(1000\theta)\,. \tag{3.52}$$

The advecting velocity field is taken to be a linear combination of 3.47 and 3.49 up to a solution time of $t = 5$. The computations are performed on a grid of size 256^2 and the time steps are of size $\Delta t = 1/100$. We showcase a gradual zoom on the solution to the point $(\lambda_0, \theta_0) = (0.75999, 1.15)$ up to a window width of 2^{-13} in the final frame. As a consequence of the functional definition of the characteristic map, each image is generated with the same number of sample points, taken to be 2000^2. We generate high resolution images within the domain up to a zoom on a window of size. Fine features that cannot be represented by the images depicting larger scales become increasingly

resolved.

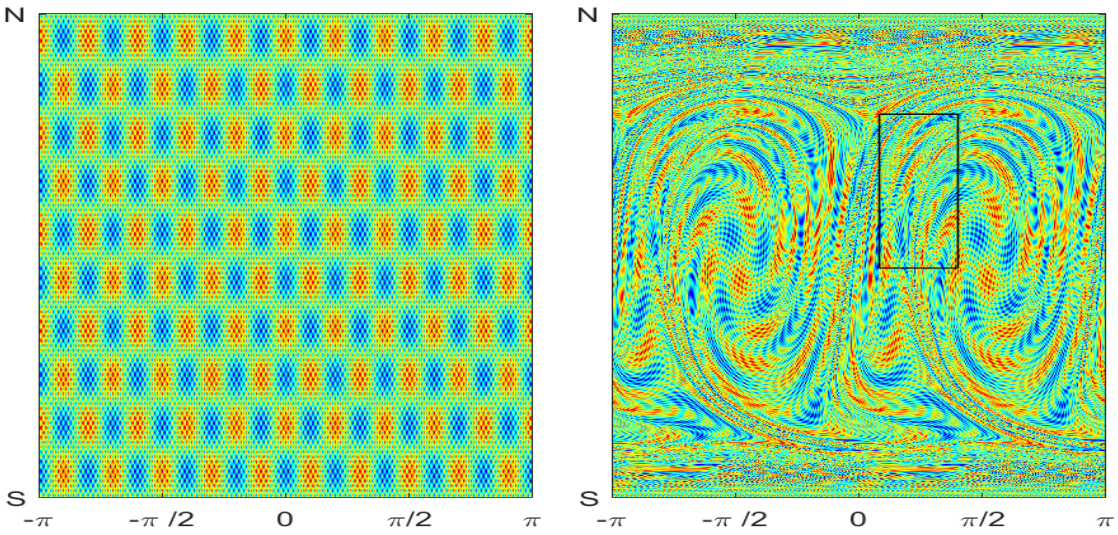

Figure 3.9: Initial condition 3.52 and the numerical solution at $t = T/2$.

The Mandelbrot set on the sphere is generated via stereographic projection with a cap of arclength 10^{-9} at the north pole. The south pole of the projection is taken to be $(-0.235125, 0.827215)$ and the axes are then scaled by a factor of 4×10^{-5}. The velocity field is taken to be 3.50 with the final solution time $T = 5$. We demonstrate a gradual zoom on a window depicted in Figure 3.11 up to a frame size of 2^{-12} for the solution at times $t = 0$ and $t = 5$. Based on the results in Figure 3.5, we expect to observe a discrepancy between in the initial condition and the final solution at a window width of 10^{-3}.

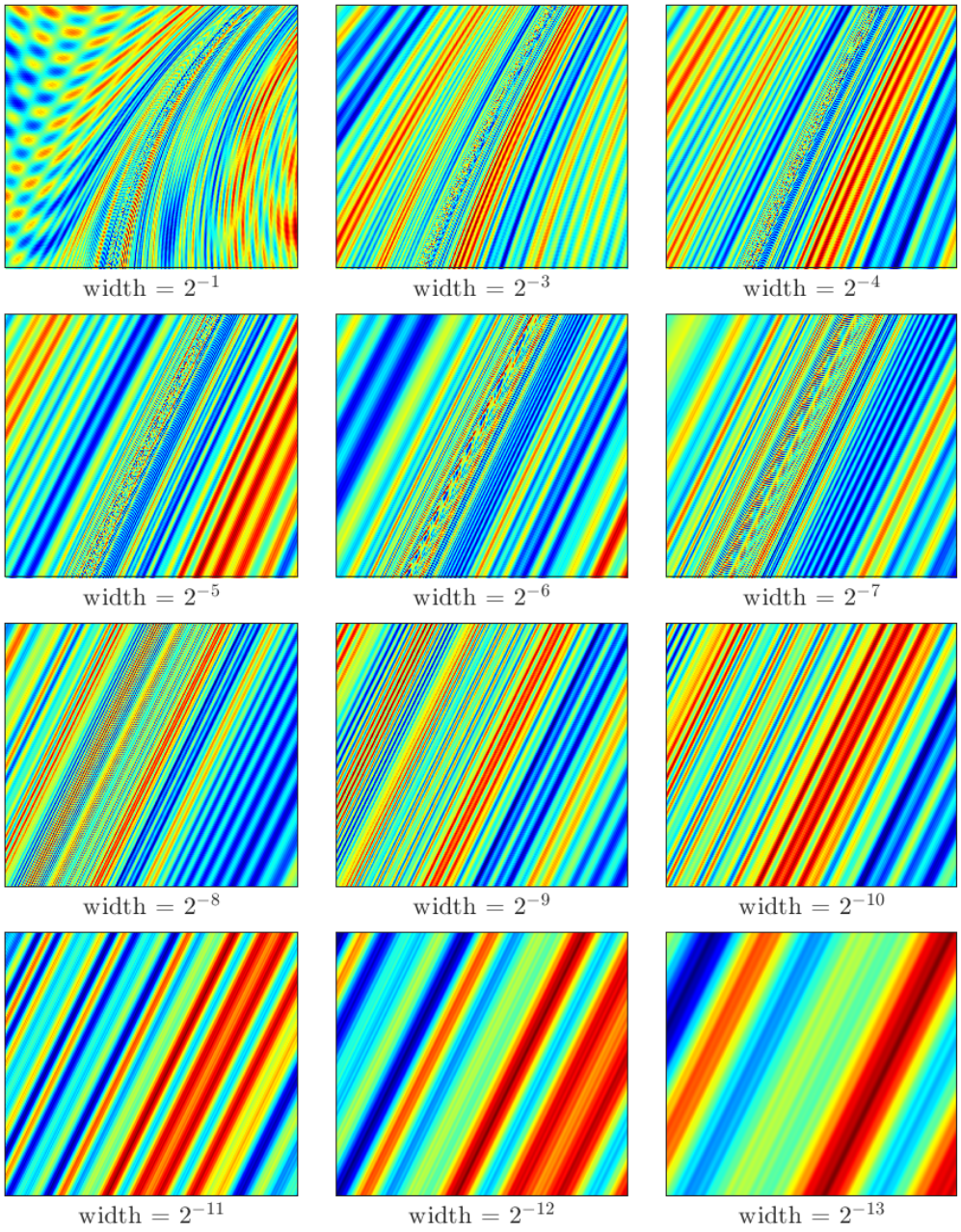

Figure 3.10: Zoom in on the final frame up to a window size of 2^{-13}.

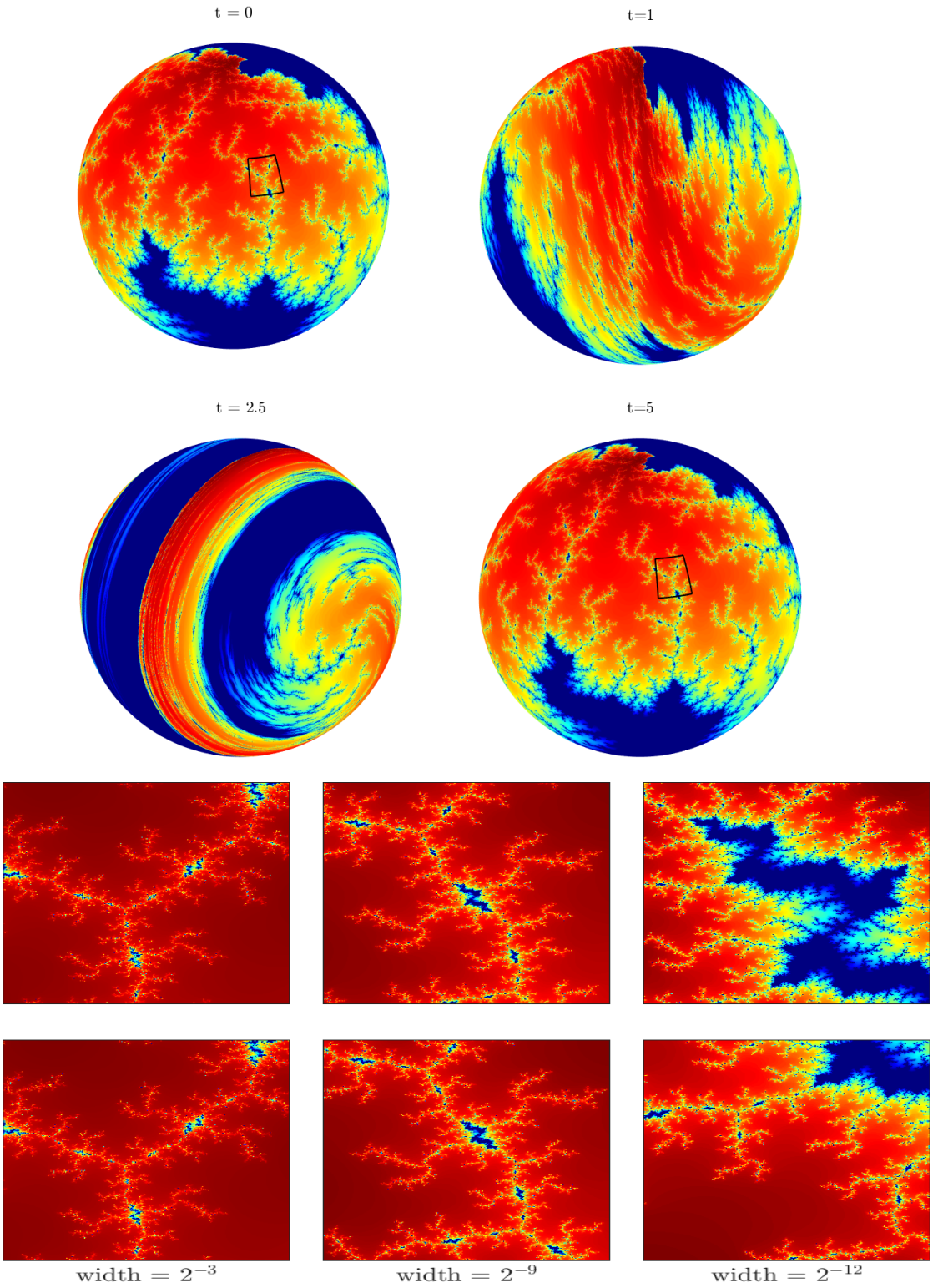

Figure 3.11: Top: Advection of the Mandelbrot set on the sphere under the velocity field 3.50. Bottom: Zoom on window depicted at times $t = 0$ (top row) and $t = 5$ (bottom row) up to a width of 2^{-12}.

Chapter 4

Aspects of the Implementation for Nonlinear Advection on a Sphere

In this concluding chapter, we investigate how to combine the double Fourier sphere method with our implementation of the CM method for linear advection on the sphere to solve the incompressible Euler equations. We discuss the limitations of using a tensor product approach to build a $C^1(\mathbb{S}^2)$ interpolant of ψ on the sphere. Furthermore, through numerical experimentation we investigate some alternative representations of the velocity field and the one-step map.

It is apparent that a representation of the velocity field with one coordinate chart will not suffice. For all the flows considered in the previous chapter, the velocity field left the poles unmoved. Since the coordinate singularity coincided with a zero of the velocity field, we were able to consider the use of a single coordinate chart. Consequently, the representation of the backward characteristic map in a single chart was also permissible. In principle to test the flexibility of a method, one could consider more general test formulations for linear advection, such as test cases 1 and 2 along an arbitrary axis of rotation passing through the origin of the embedded sphere. Moreover, one could even consider cases with prescribed motion of the poles, as in [41]. Maintaining a representation in a single coordinate chart is thus a matter of implementing a (time-dependent) coordinate transformation. One could then solve for the transport equation in a co-moving frame of reference. When the dynamics of the velocity are to be computed, as in the case of the incompressible Euler equations, these techniques could be cumbersome. Furthermore, these formulations still do not permit transport for velocity fields which are non-zero at the poles in their respective coordinate systems.

Global parameterizations of a vector field tangent to the surface of the sphere using only two coordinates will always suffer from a coordinate singularity. It is natural to instead define the velocity field either locally, using two or more coordinate charts, or globally, as embedded in $\mathbb{R}^3$. Both of these choices present different considerations for the discretization of the stream function and the local and global characteristic maps. Given our solution strategy, we find it illustrative to consider first how the definition of the stream function constrains the discretization of the velocity field. Using the extended coordinate map, the stream function admits the representation,

$$\tilde{\psi}(\lambda,\theta) = -\mathcal{F}^{-1}\{\Delta^{-1}\mathcal{F}\{\tilde{\omega}(\lambda,\theta)\}\} \tag{4.1}$$

for $(\lambda,\theta) \in [-\pi,\pi]\times[-\pi,\pi]$, where $\mathcal{F}$ represent the Fourier transform. To use the discrete Fourier transform, we require that the computational grid be evenly spaced, constraining our grid points to be equiangular in (λ,θ). The next step in the solution strategy is to project ψ into a piecewise polynomial space using a suitable projection operator defined with respect to some partition, Ω, of $\mathbb{S}^2$. We note that, in theory, we have sufficient flexibility when choosing the vertices, $\{x_i\}_{i=1}^N \in \mathbb{S}^2$ of the partition. In practice, it is computationally favourable to take the vertices to be the same grid on which the discrete Fourier transform was performed. This is due to the fact that away from the grid points the function requires N operations to evaluate.

Before considering how to construct Ω and the interpolation operator, we consider the following problem: Given points $\{x_i\}_{i=1}^N$ and data $D^\beta\psi(x_i)$, where the multiindex β is defined in terms of an index set I, with $|\beta| \leq 2$, construct a function ξ: $\mathbb{S}^2 \to \mathbb{R}$ such that

$$D^\beta\xi(x_i) = D^\beta\psi(x_i) \quad \forall\beta \in I, \forall i = 1,\dots N. \tag{4.2}$$

The definition as the data must come from the double Fourier series representation of ψ, thus we must quantify to what extent we can obtain gradient information for a function on sphere in this coordinate system. We consider $\mathbb{S}^2$ as embedded in $\mathbb{R}^3$. Denoting $\varphi : \mathbb{R}^3 \to [-\pi,\pi]\times[0,\pi]$ and the coordinate chart $x : \mathbb{R}^3 \to \mathbb{S}^2$ being the restriction of $(x,y,z) \in \mathbb{R}^3$ to $x^2+y^2+z^2 = 1$, let the coordinate representation of ψ be given by $\psi \circ x \circ \varphi^{-1}$. The gradient in the Cartesian coordinate system is then given by

$$\nabla\psi = \left[\frac{-\sin(\lambda)}{\sin(\theta)}\frac{\partial\psi}{\partial\lambda} + \cos(\lambda)\cos(\theta)\frac{\partial\psi}{\partial\theta}, \frac{\cos(\lambda)}{\sin(\theta)}\frac{\partial\psi}{\partial\lambda} + \sin(\lambda)\cos(\theta)\frac{\partial\psi}{\partial\theta}, -\sin(\theta)\frac{\partial\psi}{\partial\theta}\right] \tag{4.3}$$

Although these expressions contain unbounded terms in space, their operation in Fourier space is well-defined [63] if the grid spacing is taken using an even number of

points, see Appendix 4. As a preliminary numerical test, we validate this consideration by solving the Poisson equation for a function whose azimuthal derivative in the spherical coordinate system is multi-valued at the poles and then projecting onto its gradient in Cartesian space at the grid points. Consider the Poisson equation

$$-\Delta\psi = \omega\,, \tag{4.4}$$

with ψ given by the spherical harmonic,

$$Y_1^{-1}(\lambda,\theta) = \frac{1}{2}\sqrt{\frac{3}{\pi}}e^{-i\lambda}\sin(\theta)\,, \tag{4.5}$$

whose Cartesian gradient is given by

$$\nabla Y_1^{-1}(x,y,z) = \frac{1}{2r^3}\sqrt{\frac{3}{\pi}}\left[ixy + y^2 + z^2, -i(x^2 - ixy + z^2), -z(x - iy)\right]^T. \tag{4.6}$$

We evaluate the error at the grid points, expecting the error to be at numerical precision for all grid spacings, the results are depicted in Figure 4.1. We note that the error grows due to oversampling issues, since the spherical harmonic 4.5 has a low wave number and is well-represented using only a small number of gridpoints.

The ability to obtain derivative information in $\mathbb{R}^3$ using the expression 4.3 in frequency space offers significant flexibility for the choice of projection of ψ onto an interpolation space. Namely, we may choose from a variety of well-established interpolation schemes on the sphere [20]. From the grid points, we could partition the sphere using spherical triangles and employ a local spline interpolation method on each element. For this purpose we could then use C^1 quintic elements or C^1 cubic elements on the Clough-Tocher split, which a certain way of partitioning each spherical triangle [2]. Each of these methods requires information not solely on the grid points but along the edges of each triangle, which could compromise the optimal locality. There exists also radial basis functions as local interpolants. These have been successsfully implemented for the linear advection equation on the sphere [54]. An investigation into alternative local interpolation techniques will be a direction of future research, as we wish to use the method for other Riemannian 2-manifolds.

For our current purposes, we seek to quantify the conditions needed to project gradient and mixed partial derivative information onto a rectangular grid on the sphere such that the resulting function is $C^1(\mathbb{S}^2)$ using a tensor-product of Hermite cubics. The expression 4.3 will be well-defined for functions ψ such that $\partial_\theta\psi$ is single-valued at the poles, and $\partial_\lambda\psi$ vanishes. Using the expansion of the extended function $\tilde{\psi}$, we can determine conditions

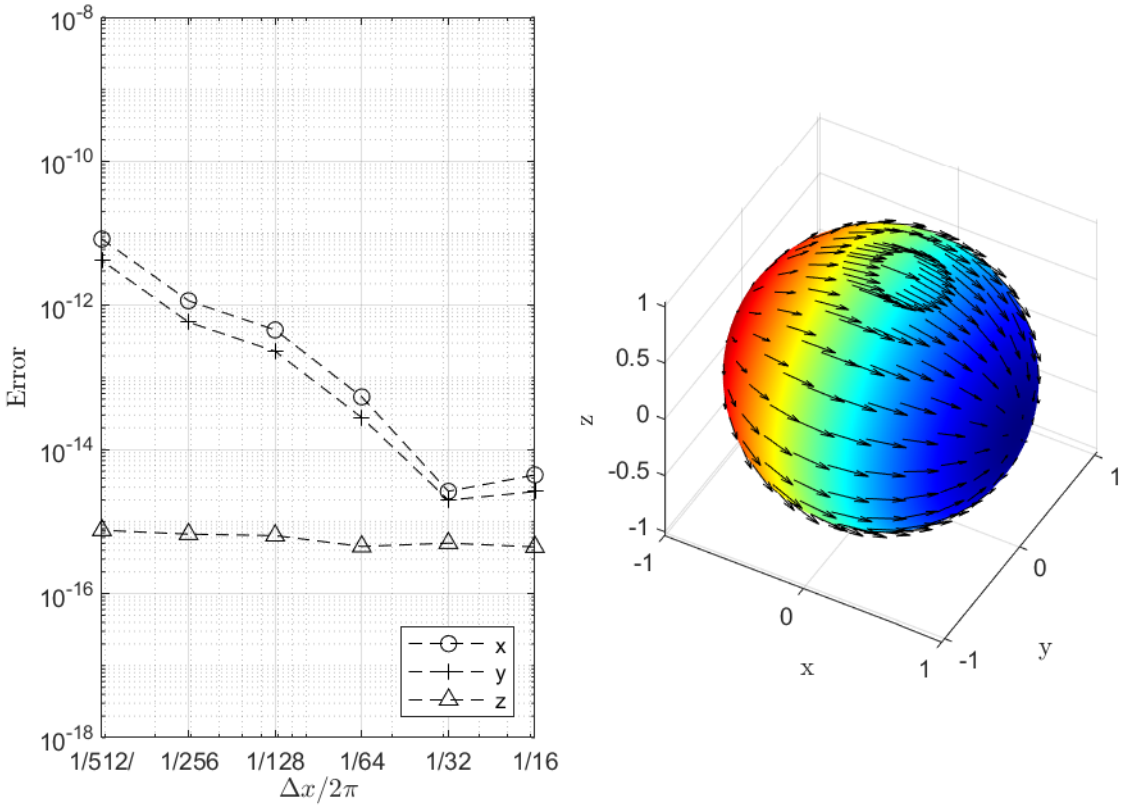

Figure 4.1: Left: Error at the grid points for the solution 4.4. Right: Visualization of Cartesian gradient data obtained form ψ using 4.3.

for which these are satisfied. Indeed, since $\tilde{\psi}$ satisfies the pole conditions, we have that,

$$\begin{aligned}\partial_\lambda \tilde{\psi}(\lambda, \pm\pi) &= \sum_{j=-\infty}^{\infty} \sum_{k=-\infty}^{\infty} \hat{\tilde{\psi}}_{j,k}(ik) e^{ik\lambda} e^{ij\pm\pi} \\ &= \sum_{k=-\infty}^{\infty} (ik) e^{ik\lambda} \sum_{j=-\infty}^{\infty} \hat{\tilde{\psi}}_{j,k} (-1)^j = 0\end{aligned} \tag{4.7}$$

and this holds analogously at $\theta = 0$. For the derivative in the θ direction, we have that

$$\begin{aligned}\partial_\theta \tilde{\psi}(\lambda, \pm\pi) &= \sum_{j=-\infty}^{\infty} \sum_{k=-\infty}^{\infty} \hat{\tilde{\psi}}_{j,k}(ij) e^{ik\lambda} e^{ij\pm\pi} \\ &= \sum_{\substack{k=-\infty \\ k\neq 0}}^{\infty} e^{ik\lambda} \sum_{j=-\infty}^{\infty} \hat{\tilde{\psi}}_{j,k}(ij)(-1)^j + \sum_{j=-\infty}^{\infty} \hat{\tilde{\psi}}_{j,0}(ij)(-1)^j \\ &= \sum_{\substack{k=-\infty \\ k\neq 0}}^{\infty} e^{ik\lambda} \sum_{j=-\infty}^{\infty} \hat{\tilde{\psi}}_{j,k}(ij)(-1)^j + C\end{aligned} \tag{4.8}$$

Since $\tilde{\psi}$ is real-valued, we have that $\hat{\psi}_{-j,k} = \overline{\hat{\psi}_{j,k}}$ $\forall j > 0$ (for notational purposes we drop the tilde). Therefore we get that

$$\begin{aligned}\sum_{j=-\infty}^{\infty} \hat{\tilde{\psi}}_{j,k}(ij)(-1)^j &= \sum_{j=0}^{\infty} (-1)^j \left((ij)\hat{\tilde{\psi}}_{j,k} - (ij)\hat{\tilde{\psi}}_{-j,k} \right) \\ &= \sum_{j=0}^{\infty} (-1)^{j+1} j \mathrm{Im}(\hat{\tilde{\psi}}_{jk})\end{aligned} \tag{4.9}$$

Using this fact, and that for $(\lambda, \theta) \in [0, \pi] \times [0, \pi]$, $\psi(\lambda, \theta) = \tilde{\psi}(\lambda, \theta) = \psi(\lambda - \pi, -\theta)$, we obtain another property the Fourier coefficients,

$$\psi(\lambda - \pi, -\theta) - \psi(\lambda, \theta) = \sum_{j=-\infty}^{\infty} \sum_{k=-\infty}^{\infty} e^{ik\lambda} e^{ij\theta} (\hat{\tilde{\psi}}_{-jk}(-1)^k - \hat{\tilde{\psi}}_{jk}) = 0\,, \tag{4.10}$$

and therefore $\hat{\tilde{\psi}}_{-jk} = (-1)^k \hat{\tilde{\psi}}_{jk}$ $\forall j, k$. Yet, since $\hat{\psi}_{-j,k} = \overline{\hat{\psi}_{j,k}}$ $\forall j > 0$, we get that

$$\begin{aligned}\mathrm{Re}\hat{\tilde{\psi}}_{jk} &= 0 \qquad \forall k \text{ odd}\,, \\ \mathrm{Im}\hat{\tilde{\psi}}_{jk} &= 0 \qquad \forall k \text{ even}\,.\end{aligned} \tag{4.11}$$

Thus we can derive a condition on the single-valuedness of the θ derivative at the poles as

$$\sum_{j=0}^{\infty} (-1)^{j+1} j \mathrm{Im}(\psi_{jk}) = \sum_{j=0}^{\infty} j \mathrm{Im}(\psi_{jk}) = 0 \quad \forall k \text{ odd}\,. \tag{4.12}$$

It should be noted that we can use these arguments straightforwardly to show that if 4.12 holds, then the mixed partial derivatives will be bounded and single valued at the poles as well.

As a numerical test, we consider an approximation of the Cartesian gradient on the sphere using the Hermite cubic constructed using the tensor-product technique. Away from the poles we may approximate the gradient values using 4.3. Due to finite-precision arithmetic, and the asymptotic behaviour of sin and cos near the poles, differences on the order of 10^{-8} cannot be resolved. Regardless, we approximate the Cartesian gradient for values within this range using only two cells, namely,

$$\begin{aligned} \nabla f|_{(0,0,1)} &\approx \lim_{h\to 0}\left(\frac{\psi(0,h)-\psi(0,0)}{h}, \frac{\psi(\pi/2,h)-\psi(\pi/2,0)}{h}, 0\right) \\ &= \left(\partial_\theta H_\Omega[f]|_{(0,0)}, \partial_\theta H_\Omega[f]|_{(\pi/2,0)}, 0\right) \end{aligned} \tag{4.13}$$

and similarly at the South pole, we obtain,

$$\nabla f|_{(0,0,-1)} \approx \left(-\partial_\theta H_\Omega[f]|_{(0,\pi)}, \partial_\theta H_\Omega[f]|_{(\pi/2,\pi)}, 0\right). \tag{4.14}$$

As a numerical test we consider interpolating 4.5 using the aforementioned procedure. The sup-norm error in the function value and gradient are approximated by evaluating at 10^6 points. The results are depicted in Figure 4.2, where we observe the expected order of convergence using the proposed method of approximation.

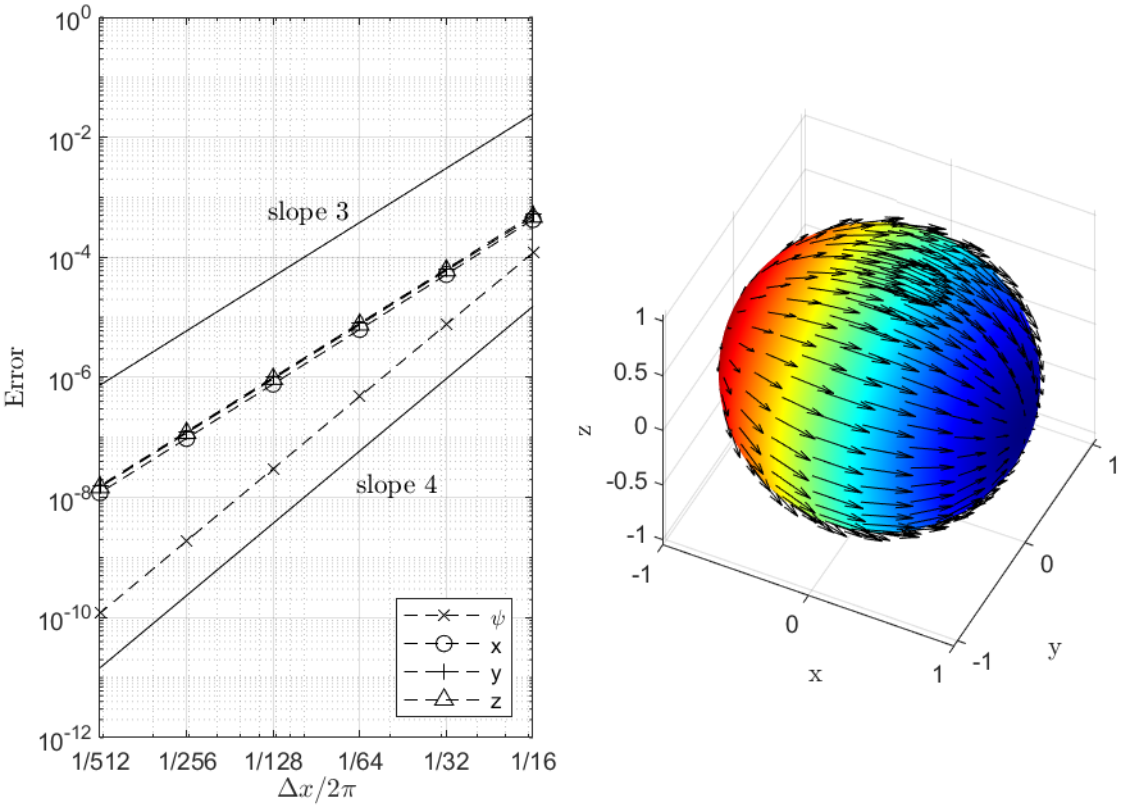

Figure 4.2: Left: Approximation of the $L^\infty(\mathbb{S}^2)$ error sampled on a grid of size 1000^2. Error in the function value and the Cartesian gradient are given. Right: Visualization of Cartesian gradient data obtained form the Hermite interpolation ψ.

Although the tensor-product interpolation technique has been demonstrated to be sufficient for the stream-function, the same behaviour is not expected for the backward-characteristic map. Indeed, it was observed in our numerical experiments that the map could become multi-valued at the poles using a mapping of the sphere to a rectangle. As we wish to approximate a diffeomorphism on the sphere, we find it desirable that our computational domain for the backward-characteristic map also be diffeomorphic to the sphere. We thus consider the feasibility of an alternative representation of the backward characteristic map.

We consider the problem of solving for the integral curves for the embedding $\mathbb{S}^2 \subset \mathbb{R}^3$. Let $\boldsymbol{x} \in \mathbb{R}^3$ such that $\|\boldsymbol{x}\| = 1$. The integral curves of the velocity field as obtained from the stream function $\psi = \psi(\boldsymbol{x}(\lambda, \theta))$ satisfy the differential equation

$$\dot{\boldsymbol{x}}(t) = u(\boldsymbol{x}(t), t) = \boldsymbol{x} \times \nabla\psi \,, \tag{4.15}$$

where ∇ is the regular gradient in Cartesian coordinates. Since $u \in T\mathbb{S}^2$ the motion should be constrained to the surface of the sphere, i.e. $\|\boldsymbol{x}(t)\| = 1$ for all time. Numerically, this constraint will not be satisfied when approximating 4.15 in Cartesian coordinates without explicitly enforcing it. We consider parameterizing the motion using rotation matrices,

$$\Lambda \in SO(3) = \left\{ M \in \mathbb{R}^{3\times 3} \,|M^T M = I, \det(M) = 1 \right\} \tag{4.16}$$

such that $x(t) = \Lambda(t)x_0$. This parameterization can be seen as transforming into the moving frame of the Lagrangian particle on the surface of the sphere, whose trajectory begins at x_0. Indeed, in the moving frame of reference, the particle's motion is characterized by the entire sphere rotating. This action is naturally represented using elements of $SO(3)$. We consider the 'hat-map', allowing us to map to the Lie algebra $\mathfrak{so}(3)$ of $SO(3)$, which is the set of skew-symmetric matrices. The hat map $\hat{\cdot} : \mathbb{R}^3 \to \mathfrak{so}(3)$ acts on $\boldsymbol{x} \in \mathbb{R}^3$

$$\boldsymbol{x} \mapsto \begin{bmatrix} 0 & -x_3 & x_2 \\ x_3 & 0 & -x_1 \\ -x_2 & x_1 & 0 \end{bmatrix} \tag{4.17}$$

such that for $y \in \mathbb{R}^3$,

$$\boldsymbol{x} \times \boldsymbol{y} = \hat{\boldsymbol{x}}\boldsymbol{y} \,. \tag{4.18}$$

Thus, for an initial point $\boldsymbol{x}_i \in \mathbb{R}^3$, $\|x\| = 1$, the evolution of $\boldsymbol{x}_i$ governed by 4.15 can be

determined by the following differential equation on $SO(3)$,

$$\begin{aligned}\dot{\boldsymbol{x}}(t) &= \dot{\Lambda}(t)\boldsymbol{x}_i = \Lambda\boldsymbol{x}_i \times \nabla\psi(\boldsymbol{x}(\lambda,\theta),t) \\ &= -\nabla\hat{\psi}(\boldsymbol{x}(\lambda,\theta),t)(t)x_0\,.\end{aligned} \tag{4.19}$$

Letting $\nabla\hat{\psi}(\boldsymbol{x}(\lambda,\theta),t) = \Omega(\Lambda(t)x_0,t)$, we obtain the following differential equation on $SO(3)$,

$$\dot{\Lambda}(t) = -\Omega(\Lambda(t)x_0,t)\Lambda(t). \tag{4.20}$$

As a proof of concept, we consider the solution of 4 using a velocity field defined from a Hermite interpolation of the stream function on the sphere and an RK3 integration scheme on $\mathbb{R}^{3\times3}$ for the coefficients of Λ. We consider the stream function,

$$\psi(\lambda,\theta) = 2\pi(\cos(\theta)\cos(\alpha) - \cos(\lambda)\sin(\theta)\sin(\alpha))\,, \tag{4.21}$$

whose velocity field defines a solid body rotation about an axis an angle α away from the north pole in the direction of the $-x$-axis [70]. We consider velocity fields defined for the stream function 4.21 for $\alpha = \pi/4, \pi/2$, depicted in Figure 4.3. We consider convergence tests for the solution of 4 at 100 staggered points on the sphere to a final integration time of $T = 1$, corresponding to one full rotation. The error is computed as the ℓ^∞ error at the grid points. Convergence in time is evaluated using a velocity field defined from the Hermite interpolant of ψ on a 1000×1000 grid points. The convergence in space is evaluated successively refined grid for the Hermite interpolant and a time step of size $\Delta t = 1/300$. The results of the numerical test are depicted in Figure 4.4.

Although we have not provided estimates for the expected rate of convergence, we remark that we do not expect to observe to the same convergence for an RK3 integration scheme for elements $\Lambda \in SO(3)$. Indeed, using a simple Euler step,

$$\frac{\Lambda^{n+1} - \Lambda^n}{\Delta t} = \Omega(\Lambda^n x_0, t^n)\Lambda^n\,, \tag{4.22}$$

we observe that,

$$\left(\Lambda^{n+1}\right)^T\left(\Lambda^{n+1}\right)^T = I + \Delta t^2\left(\Lambda^n\right)^T(\Omega\Omega^T)^n\Lambda^n \notin SO(3). \tag{4.23}$$

where we have used the skew-symmetry property of Ω to cancel the first order terms. Since, RK3 uses a convex combination of Euler steps and Λ acts multiplicatively on x_0 throughout the time integration, we do not expect the same order of convergence. Furthermore, the fact that Λ leaves the group can introduce non-linearities in the differential equation we seek to solve, leading to possible issues with consistency [31].

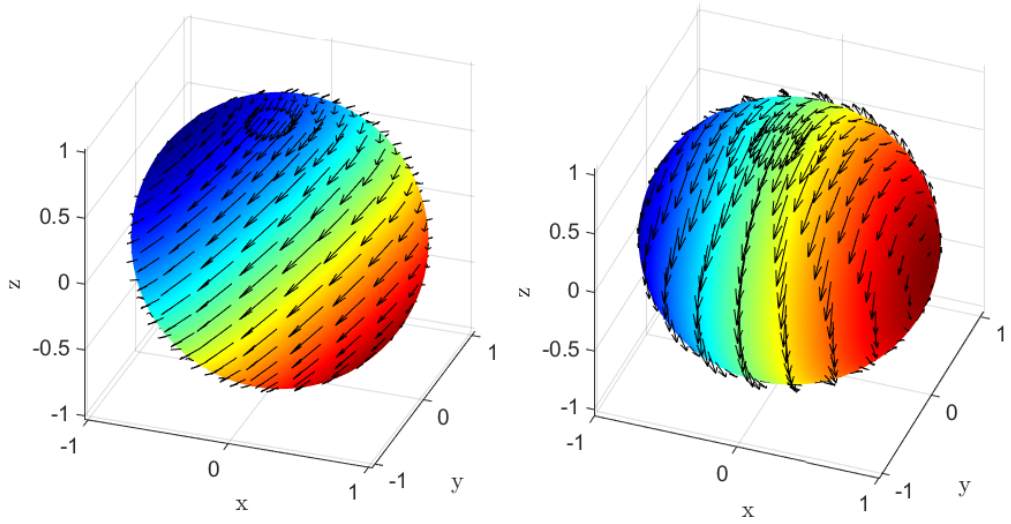

Figure 4.3: Left: Velocity field resulting from 4.21 with $\alpha = \pi/4$. Right: Velocity field resulting from 4.21 with $\alpha = \pi/2$.

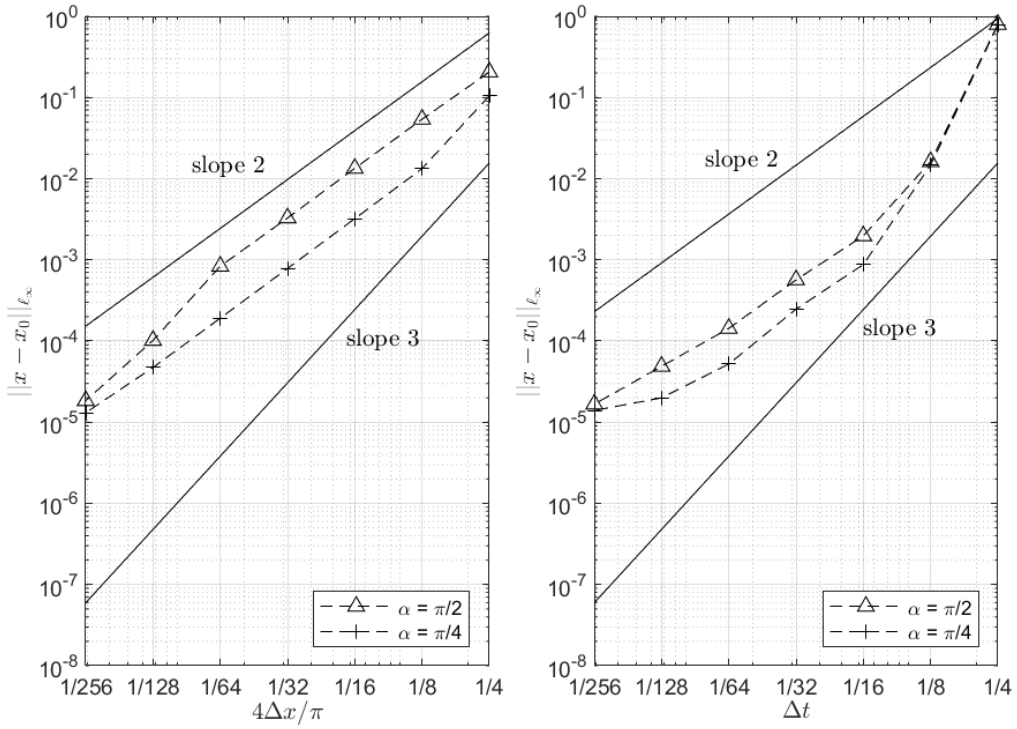

Figure 4.4: Left: Convergence in space for the solution to 4.20 using the velocities fields depicted in 4.3. Right: Convergence in time.

Further analysis of methods to will need be done in order to accurately quantify the convergence seen in 4.4. A direction of research in the immediate future will be to use the techniques of geometric integration to solve in order to preserve the group property through the integration. It would be interesting to couple a geometric integration scheme, with the interpolation techniques in [24] for functions taking value in $SO(3)$ or in the space of unit quaternions using Cayley-Klein parameters. This would provide a means of evolving a characteristic map taking values in the Lie groups $SO(3)$ or $SU(2)$. These considerations would offer a novel numerical method for the incompressible Euler equations and present a wealth of interesting research directions to explore further.

Conclusion and Outlook

This thesis serves to provide a framework for the solution of the incompressible Euler equations on a two dimensional sphere using the Characteristic Mapping method. We have discussed the vorticity-stream formulation of Euler's equations on a sphere, upon which the solution strategy was built. An implementation to solve for the stream function using the spherical Poisson equation, with vorticity as forcing function, using the Double Fourier Sphere method was presented and tested. We then detailed an implementation of the CM method for the solution of the linear advection equation on a sphere. Our numerics were tested against a series of canonical test cases and the method's ability to advect arbitrary sets and obtain arbitrary resolution were highlighted. The thesis concluded with an investigation into combining these two numerical methods in order to solve the incompressible Euler equations on a sphere.

Difficulties relating to the spherical geometry have been demonstrated to be alleviated by considering the evolution of the one-step map in the space of special orthogonal matrices. Furthermore, it was shown that the definition of the stream-function on a rectangular domain was not restrictive. We demonstrated that this allowed for a high-order approximation of the velocity field in a Cartesian coordinate system. The significant amount of flexibility identified when combining these two numerical methods will ultimately be narrowed down by considerations of efficiency and accuracy. The immediate next steps for this research are to investigate the approximation properties of Lie group integrators and interpolation techniques for functions taking values in the space of unit quaternions or special orthogonal matrices.

Bibliography

[1] Ralph Abraham, Jerrold E Marsden, and Tudor Ratiu. *Manifolds, tensor analysis, and applications*, volume 75. Springer Science & Business Media, 2012.

[2] Peter Alfeld, Marian Neamtu, and Larry L Schumaker. Fitting scattered data on sphere-like surfaces using spherical splines. *Journal of Computational and Applied Mathematics*, 73(1):5–43, 1996.

[3] Myles R Allen, Peter A Stott, John FB Mitchell, Reiner Schnur, and Thomas L Delworth. Quantifying the uncertainty in forecasts of anthropogenic climate change. *Nature*, 407(6804):617–620, 2000.

[4] Samuel M Allen and John W Cahn. A microscopic theory for antiphase boundary motion and its application to antiphase domain coarsening. *Acta metallurgica*, 27(6):1085–1095, 1979.

[5] LA Barba, A Leonard, and CB Allen. Advances in viscous vortex methods—meshless spatial adaption based on radial basis function interpolation. *International Journal for Numerical Methods in Fluids*, 47(5):387–421, 2005.

[6] J Thomas Beale and Andrew Majda. High order accurate vortex methods with explicit velocity kernels. *Journal of Computational Physics*, 58(2):188–208, 1985.

[7] Pierre Bénard and Michael R Glinton. Circumventing the pole problem of reduced lat–lon grids with local schemes. part i: Analysis and model formulation. *Quarterly Journal of the Royal Meteorological Society*, 145(721):1377–1391, 2019.

[8] Marsha J Berger, Phillip Colella, et al. Local adaptive mesh refinement for shock hydrodynamics. *Journal of computational Physics*, 82(1):64–84, 1989.

[9] Peter Bosler, Lei Wang, Christiane Jablonowski, and Robert Krasny. A lagrangian particle/panel method for the barotropic vorticity equations on a rotating sphere. *Fluid Dynamics Research*, 46(3):031406, 2014.

[10] Peter A Bosler. *Particle Methods for Geophysical Flow on the Sphere.* PhD thesis, 2013.

[11] Peter A Bosler, James Kent, Robert Krasny, and Christiane Jablonowski. A lagrangian particle method with remeshing for tracer transport on the sphere. *Journal of Computational Physics*, 340:639–654, 2017.

[12] Bin Cheng and Alex Mahalov. Euler equation on a fast rotating sphere—time-averages and zonal flows. *European Journal of Mechanics-B/Fluids*, 37:48–58, 2013.

[13] Hyeong-Bin Cheong. Double fourier series on a sphere: Applications to elliptic and vorticity equations. *Journal of Computational Physics*, 157(1):327–349, 2000.

[14] James W Cooley and John W Tukey. An algorithm for the machine calculation of complex fourier series. *Mathematics of computation*, 19(90):297–301, 1965.

[15] CJ Cotter, J Frank, and S Reich. The remapped particle-mesh semi-lagrangian advection scheme. *Quarterly Journal of the Royal Meteorological Society: A journal of the atmospheric sciences, applied meteorology and physical oceanography*, 133(622):251–260, 2007.

[16] Francine Desharnais and André Robert. Errors near the poles generated by a semi-lagrangian integration scheme in a global spectral model. *Atmosphere-Ocean*, 28(2):162–176, 1990.

[17] Paul Dierckx. Algorithms for smoothing data on the sphere with tensor product splines. *Computing*, 32(4):319–342, 1984.

[18] Leonhard Euler. Principia motus fluidorum. *Novi commentarii academiae scientiarum Petropolitanae*, pages 271–311, 1761.

[19] Gregory E Fasshauer. Hermite interpolation with radial basis functions on spheres. *Advances in Computational Mathematics*, 10(1):81, 1999.

[20] Gregory E Fasshauer and Larry L Schumaker. Scattered data fitting on the sphere. *Mathematical Methods for Curves and Surfaces II*, pages 117–166, 1998.

[21] Natasha Flyer and Erik Lehto. Rotational transport on a sphere: Local node refinement with radial basis functions. *Journal of Computational Physics*, 229(6):1954–1969, 2010.

[22] Matteo Frigo and Steven G. Johnson. FFTW: Fastest Fourier Transform in the West, January 2012.

[23] E Garcıa-Melendo and A Sánchez-Lavega. A study of the stability of jovian zonal winds from hst images: 1995–2000. *Icarus*, 152(2):316–330, 2001.

[24] Evan S Gawlik and Melvin Leok. Embedding-based interpolation on the special orthogonal group. *SIAM Journal on Scientific Computing*, 40(2):A721–A746, 2018.

[25] John D Gibbon. The three-dimensional euler equations: Where do we stand? *Physica D: Nonlinear Phenomena*, 237(14-17):1894–1904, 2008.

[26] Lucas M Harris, Peter H Lauritzen, and Rashmi Mittal. A flux-form version of the conservative semi-lagrangian multi-tracer transport scheme (cslam) on the cubed sphere grid. *Journal of Computational Physics*, 230(4):1215–1237, 2011.

[27] Cyrill W Hirt, Anthony A Amsden, and JL Cook. An arbitrary lagrangian-eulerian computing method for all flow speeds. *Journal of computational physics*, 14(3):227–253, 1974.

[28] Eigil Kaas, Brian Sørensen, Peter H Lauritzen, and Ayoe Buus Hansen. A hybrid eulerian–lagrangian numerical scheme for solving prognostic equations in fluid dynamics. *Geoscientific Model Development*, 6(6):2023–2047, 2013.

[29] Haruhiko Kohno and Jean-Christophe Nave. A new method for the level set equation using a hierarchical-gradient truncation and remapping technique. *Computer Physics Communications*, 184(6):1547–1554, 2013.

[30] Peter H Lauritzen, Ramachandran D Nair, and Paul A Ullrich. A conservative semi-lagrangian multi-tracer transport scheme (cslam) on the cubed-sphere grid. *Journal of Computational Physics*, 229(5):1401–1424, 2010.

[31] Debra Lewis and Nilima Nigam. Geometric integration on spheres and some interesting applications. *Journal of Computational and Applied Mathematics*, 151(1):141–170, 2003.

[32] Yibao Li, Hyun Geun Lee, Darae Jeong, and Junseok Kim. An unconditionally stable hybrid numerical method for solving the allen–cahn equation. *Computers & Mathematics with Applications*, 60(6):1591–1606, 2010.

[33] Shian-Jiann Lin. A "vertically lagrangian" finite-volume dynamical core for global models. *Monthly Weather Review*, 132(10):2293–2307, 2004.

[34] Xu-Dong Liu, Stanley Osher, Tony Chan, et al. Weighted essentially non-oscillatory schemes. *Journal of computational physics*, 115(1):200–212, 1994.

[35] Adrien Magni and Georges-Henri Cottet. Accurate, non-oscillatory, remeshing schemes for particle methods. *Journal of Computational Physics*, 231(1):152–172, 2012.

[36] Olivier Mercier, Xi-Yuan Yin, and Jean-Christophe Nave. The characteristic mapping method for the linear advection of arbitrary sets. *SIAM Journal on Scientific Computing*, 42(3):A1663–A1685, 2020.

[37] Philip E Merilees. The pseudospectral approximation applied to the shallow water equations on a sphere. *Atmosphere*, 11(1):13–20, 1973.

[38] Hadrien Montanelli and Yuji Nakatsukasa. Fourth-order time-stepping for stiff pdes on the sphere. *SIAM Journal on Scientific Computing*, 40(1):A421–A451, 2018.

[39] James M Murphy, David MH Sexton, David N Barnett, Gareth S Jones, Mark J Webb, Matthew Collins, and David A Stainforth. Quantification of modelling uncertainties in a large ensemble of climate change simulations. *Nature*, 430(7001):768–772, 2004.

[40] Ramachandran Nair, Jean Côté, and Andrew Staniforth. Cascade interpolation for semi-lagrangian advection over the sphere. *Quarterly Journal of the Royal Meteorological Society*, 125(556):1445–1468, 1999.

[41] Ramachandran D Nair and Christiane Jablonowski. Moving vortices on the sphere: A test case for horizontal advection problems. *Monthly Weather Review*, 136(2):699–711, 2008.

[42] Ramachandran D Nair and Peter H Lauritzen. A class of deformational flow test cases for linear transport problems on the sphere. *Journal of Computational Physics*, 229(23):8868–8887, 2010.

[43] Ramachandran D Nair and Bennert Machenhauer. The mass-conservative cell-integrated semi-lagrangian advection scheme on the sphere. *Monthly Weather Review*, 130(3):649–667, 2002.

[44] Jean-Christophe Nave, Rodolfo Ruben Rosales, and Benjamin Seibold. A gradient-augmented level set method with an optimally local, coherent advection scheme. *Journal of Computational Physics*, 229(10):3802–3827, 2010.

[45] Henrik O Nordmark. Rezoning for higher order vortex methods. *Journal of Computational Physics*, 97(2):366–397, 1991.

[46] Steven A Orszag. Fourier series on spheres. *Monthly Weather Review*, 102(1):56–75, 1974.

[47] Stanley Osher, Ronald Fedkiw, and K Piechor. Level set methods and dynamic implicit surfaces. *Appl. Mech. Rev.*, 57(3):B15–B15, 2004.

[48] Mirta Perlman. On the accuracy of vortex methods. *Journal of Computational Physics*, 59(2):200–223, 1985.

[49] Michael J Prather, Xin Zhu, Susan E Strahan, Stephen D Steenrod, and Jose M Rodriguez. Quantifying errors in trace species transport modeling. *Proceedings of the National Academy of Sciences*, 105(50):19617–19621, 2008.

[50] Cornelius Rampf, Eleonora Villa, Daniele Bertacca, and Marco Bruni. Lagrangian theory for cosmic structure formation with vorticity: Newtonian and post-friedmann approximations. *Physical Review D*, 94(8):083515, 2016.

[51] Vladimir Rokhlin and Mark Tygert. Fast algorithms for spherical harmonic expansions. *SIAM Journal on Scientific Computing*, 27(6):1903–1928, 2006.

[52] Larry L Schumaker and Cornelis Traas. Fitting scattered data on spherelike surfaces using tensor products of trigonometric and polynomial splines. *Numerische Mathematik*, 60(1):133–144, 1991.

[53] Benjamin Seibold and Jean-Christophe Nave Rodolfo R. Rosales. Jet schemes for advection problems. *Discrete & Continuous Dynamical Systems - B*, 17:1229, 2012.

[54] Varun Shankar and Grady B Wright. Mesh-free semi-lagrangian methods for transport on a sphere using radial basis functions. *Journal of Computational Physics*, 366:170–190, 2018.

[55] Chi-Wang Shu and Stanley Osher. Efficient implementation of essentially non-oscillatory shock-capturing schemes. *Journal of computational physics*, 77(2):439–471, 1988.

[56] Frederick G Shuman. On certain truncation errors associated with spherical coordinates. *Journal of Applied Meteorology*, 9(4):564–570, 1970.

[57] Richard Mikael Slevinsky. Fast and backward stable transforms between spherical harmonic expansions and bivariate fourier series. *Applied and Computational Harmonic Analysis*, 2017.

[58] Andrew Staniforth and Jean Côté. Semi-lagrangian integration schemes for atmospheric models—a review. *Monthly weather review*, 119(9):2206–2223, 1991.

[59] Paul N Swarztrauber. On the spectral approximation of discrete scalar and vector functions on the sphere. *SIAM Journal on Numerical Analysis*, 16(6):934–949, 1979.

[60] Paul N Swarztrauber. The approximation of vector functions and their derivatives on the sphere. *SIAM Journal on Numerical Analysis*, 18(2):191–210, 1981.

[61] PN Swarztrauber. On the approximation of discrete scalar and vector functions on the sphere. *SIAM J. Numer. Anal*, 7:934–949, 1970.

[62] John Thuburn and Michael E McIntyre. Numerical advection schemes, cross-isentropic random walks, and correlations between chemical species. *Journal of Geophysical Research: Atmospheres*, 102(D6):6775–6797, 1997.

[63] Alex Townsend, Heather Wilber, and Grady B Wright. Computing with functions in spherical and polar geometries i. the sphere. *SIAM Journal on Scientific Computing*, 38(4):C403–C425, 2016.

[64] Mark Tygert. Fast algorithms for spherical harmonic expansions ii. *Journal of Computational Physics*, 227(8):4260–4279, 2008.

[65] Mark Tygert. Fast algorithms for spherical harmonic expansions iii. *Journal of Computational Physics*, 229(18):6181–6192, 2010.

[66] Naum IAkovlevich Vilenkin. *Special functions and the theory of group representations*, volume 22. American Mathematical Soc., 1978.

[67] Pierre Welander. Studies on the general development of motion in a two-dimensional, ideal fluid. *Tellus*, 7(2):141–156, 1955.

[68] David L Williamson. The evolution of dynamical cores for global atmospheric models. *Journal of the Meteorological Society of Japan. Ser. II*, 85:241–269, 2007.

[69] David L Williamson and Gerald L Browning. Comparison of grids and difference approximations for numerical weather prediction over a sphere. *Journal of Applied Meteorology*, 12(2):264–274, 1973.

[70] David L Williamson, John B Drake, James J Hack, Rüdiger Jakob, and Paul N Swarztrauber. A standard test set for numerical approximations to the shallow water equations in spherical geometry. *Journal of Computational Physics*, 102(1):211–224, 1992.

[71] David L Williamson and Philip J Rasch. Two-dimensional semi-lagrangian transport with shape-preserving interpolation. *Monthly Weather Review*, 117(1):102–129, 1989.

[72] Jianping Xiao, Lei Wang, and John P Boyd. Rbf-vortex methods for the barotropic vorticity equation on a sphere. *Journal of Computational Physics*, 285:208–225, 2015.

[73] Samuel YK Yee. Solution of poisson's equation on a sphere by truncated double fourier series. *Monthly Weather Review*, 109(3):501–505, 1981.

[74] Xi-Yuan Yin, Olivier Mercier, Badal Yadav, Kai Schneider, and Jean-Christophe Nave. A characteristic mapping method for the two-dimensional incompressible euler equations. *arXiv preprint arXiv:1910.10841*, 2019.

[75] Victor Iosifovich Yudovich. The flow of a perfect, incompressible liquid through a given region. *SPhD*, 7:789, 1963.

Appendix A: Fourier multiplication matrices

In this appendix we give the construction of the matrices representing certain operators acting on frequency space. Furthermore, we seek to determine when these matrices are singular, as we will often require their inverses. As an initial motivation, we first consider the construction of the matrices representing the partial differential operators. Since most FFT codes hold the coefficients in a form of

$$\hat{u} = \left(\frac{\hat{u}_{n/2}}{2} + \frac{\hat{u}_{-n/2}}{2} = \hat{u}_{-n/2}, \hat{u}_{-n/2+1}, \ldots, \hat{u}_{n/2-1} \right) , \tag{4.24}$$

a naive application of Fourier differentiation will not result in the first element being zero, but would rather yield a $(in/2)e^{in\phi}$ mode. To remedy this issue and make the operation of differentiation more systematic, we first project the coefficient vector into a space with $n+1$ modes, multiply with the Fourier differentiation matrix on the $n+1$ modes and then project back to a space with n modes once more. The whole operation can be expressed as the product of three matrices,

$$\mathbf{D}_n = \mathbf{Q}\mathbf{D}_{n+1}\mathbf{P} \tag{4.25}$$

where $\mathbf{P}$ is given by

$$\mathbf{P} = \begin{bmatrix} \frac{1}{2} & & & \\ & 1 & & \\ & & \ddots & \\ & & & 1 \\ \frac{1}{2} & & & 0 \end{bmatrix} , \tag{4.26}$$

the Fourier differentiation matrix is given by

$$\mathbf{D}_{n+1} = \mathrm{diag}((-in/2, -i(n/2+1), \ldots, i(n/2-1))) \tag{4.27}$$

and $\mathbf{Q}$ by

$$\mathbf{Q} = \begin{bmatrix} 1 & & & & 1 \\ & 1 & & & \\ & & \ddots & & \\ & & & 1 & 0 \end{bmatrix}. \tag{4.28}$$

The matrix representation of multiplication by trigonometric functions uses a similar approach as for the differentiation matrices, by first projecting into a larger space of coefficients. We first note that

$$\sin^2(\theta) = \frac{1}{2} - \frac{1}{4}e^{-2i\theta} - \frac{1}{4}e^{2i\theta}, \tag{4.29}$$

and

$$\cos(\theta)\sin(\theta) = -\frac{i}{4}e^{2i\theta} + \frac{i}{4}e^{-2i\theta}. \tag{4.30}$$

Thus multiplying by these functions has the effect of increasing the length of Fourier representation by four, increasing the number of frequencies initially present in the function they are multiplying. The matrix, $\mathbf{M}_{\sin^2}$, describing the multiplication is given by

$$\mathbf{M}_{\sin^2} = \begin{bmatrix} \frac{1}{2} & 0 & -\frac{1}{4} & & & & \\ 0 & \frac{1}{2} & 0 & -\frac{1}{4} & & & \\ -\frac{1}{4} & 0 & \ddots & \ddots & \ddots & & \\ & -\frac{1}{4} & \ddots & \ddots & \ddots & \ddots & \\ & & \ddots & \ddots & \ddots & \ddots & -\frac{1}{4} \\ & & & \ddots & \ddots & \ddots & 0 \\ & & & & -\frac{1}{4} & 0 & \frac{1}{2} \end{bmatrix}, \tag{4.31}$$

and similarly, the matrix $\mathbf{M}_{\sin\cos}$ is given by

$$\mathbf{M}_{\sin\cos} = \begin{bmatrix} 0 & 0 & -\frac{i}{4} & & & & \\ 0 & 0 & 0 & -\frac{i}{4} & & & \\ \frac{i}{4} & 0 & \ddots & \ddots & \ddots & & \\ & \frac{i}{4} & \ddots & \ddots & \ddots & \ddots & \\ & & \ddots & \ddots & \ddots & \ddots & -\frac{i}{4} \\ & & & \ddots & \ddots & \ddots & 0 \\ & & & & \frac{i}{4} & 0 & 0 \end{bmatrix}. \tag{4.32}$$

The full multiplication matrices are then expressed as

$$\mathbf{T}_f = \mathbf{Q}\mathbf{M}_f[:, k : m + 1 + 2]\mathbf{P}\,, \tag{4.33}$$

where f is the corresponding trigonometric function we seek to represent, and k is the number of added modes needed to represent the multiplication. We have used a notation for slicing consistent with NumPy arrays for the matrix $\mathbf{M}$. The matrix $\mathbf{Q}$, for $k = 2$, is instead given by

$$\mathbf{Q} = \begin{bmatrix} 0 & 0 & 1 & & & & 1 & 0 & 0 \\ & & & 1 & & & & & \\ & & & & \ddots & & & & \\ & & & & & 1 & 0 & 0 & 0 \end{bmatrix}. \tag{4.34}$$

We now seek to establish when the matrices $\mathbf{T}_f$ can be inverted. In particular, since for the Laplacian and gradient only a $1/\sin^2(\theta)$ and $1/\sin(\theta)$ are needed, we only focus on the invertibility of their respective coefficient multiplication matrix representations. For $M_{\sin(\theta)}$

$$\mathbf{M}_{\sin} = \frac{i}{2}\begin{bmatrix} 0 & 1 & & & \\ -1 & 0 & 1 & & \\ & \ddots & \ddots & \ddots & \\ & \ddots & \ddots & 0 & 1 \\ & & & -1 & 0 \end{bmatrix}. \tag{4.35}$$

We recognize this as a tridiagonal Toeplitz matrix, whose eigenvalues are given by $\lambda_\ell = \cos(\pi\ell/(m+1)$ which are non zero for m even.

The matrix $\mathbf{T}_{\sin^2(\theta)}$ is given by

$$\mathbf{T}_{\sin^2} = \begin{bmatrix} \frac{1}{2} & 0 & -\frac{1}{4} & & & -\frac{1}{4} & 0 \\ 0 & \frac{1}{2} & 0 & -\frac{1}{4} & & & \\ -\frac{1}{8} & 0 & \ddots & \ddots & \ddots & & \\ & -\frac{1}{4} & \ddots & \ddots & \ddots & \ddots & \\ & & \ddots & \ddots & \ddots & \ddots & -\frac{1}{4} \\ -\frac{1}{8} & & & -\frac{1}{4} & \ddots & \frac{1}{2} & 0 \\ 0 & \dots & \dots & \cdots & -\frac{1}{4} & 0 & \frac{1}{2} \end{bmatrix}. \tag{4.36}$$

In order to observe the non-singularity of the matrix $\mathbf{T}_{\sin^2(\theta)}$, we note that the matrix can be brought into a lower triangular form by reducing all entries along the second upper

diagonal, with all non-zero entries along the diagonal. The reduced matrix, denoted A, is almost triangular with non-zero $(1, n-1)$ entry being $-1/4$. Writing $A = B + uv^T$, where B is lower triangular, $u = [i/2, 0, \ldots, 0]$, and $v = [0, \ldots, i/2, 0]$, we get that $\det(\mathbf{T}_{\sin^2(\theta)}) = \det(A) = \det\left(B + uv^T\right) = (1 + v^T B^{-1} u)\det(B) = (1 - [B^{-1}]_{(n-1,1)}/4)\det(B)$. The diagonal of the matrix B is given by $\mathrm{diag}(B) = [-9/2^{m/2+6}, 3/8, 3/8, \ldots, 3/8, 1/2]$. Note that $[B^{-1}]_{(n-1,1)} = (\det B)^{-1}[C^T]_{(n-1,1)} = (\det B)^{-1}[C^T]_{(n-1,1)} = (\det B)^{-1}[C]_{(1,n-1)}$ where C is the cofactor matrix of B . The result $[B^{-1}]_{(n-1,1)} \neq 4$ was verified numerically. We note that an explicit formula for this entry can be derived using only the reduced matrix A. Write the triangular matrix as $B = D(I + D^{-1}N)$ where D is a diagonal matrix and N is a strictly lower triangular matrix with zeroes along the diagonal. Using the fact that $N^n = 0$, factoring the polynomial $1 - t^n = (1 - t)(1 + t + t^2 + \cdots t^{n-1})$, and evaluating at $t = -D^{-1}N$, the inverse of B is given by

$$B^{-1} = (I + D^{-1}N)^{-1}D^{-1} = D^{-1} + \sum_{k=0}^{n-1}(-1)^k \left(D^{-1}N\right)^k D^{-1} \tag{4.37}$$

and thus,

$$[B^{-1}]_{(n-1,1)} = \sum_{k=1}^{n-1}(-1)^k e_{n-1}^T \left(D^{-1}N\right)^k D^{-1}e_1\,. \tag{4.38}$$